



저작자표시-비영리-변경금지 2.0 대한민국

이용자는 아래의 조건을 따르는 경우에 한하여 자유롭게

- 이 저작물을 복제, 배포, 전송, 전시, 공연 및 방송할 수 있습니다.

다음과 같은 조건을 따라야 합니다:



저작자표시. 귀하는 원저작자를 표시하여야 합니다.



비영리. 귀하는 이 저작물을 영리 목적으로 이용할 수 없습니다.



변경금지. 귀하는 이 저작물을 개작, 변형 또는 가공할 수 없습니다.

- 귀하는, 이 저작물의 재이용이나 배포의 경우, 이 저작물에 적용된 이용허락조건을 명확하게 나타내어야 합니다.
- 저작권자로부터 별도의 허가를 받으면 이러한 조건들은 적용되지 않습니다.

저작권법에 따른 이용자의 권리는 위의 내용에 의하여 영향을 받지 않습니다.

이것은 [이용허락규약\(Legal Code\)](#)을 이해하기 쉽게 요약한 것입니다.

[Disclaimer](#)

Ph. D. DISSERTATION

A Study on the Correlations between anti phase domain and luminescence characteristics of alpha-Ga₂O₃ using deep-UV Cathodoluminescence stage for Transmission Electron Microscopy

고 에너지 영역 투과전자현미경용 음극 형광 분석 시스템을
통한 alpha-Ga₂O₃ 기반 소자의 역상 도메인과 발광 특성과의
상관관계에 대한 연구

by

Yong-Hee Lee

August 2023

Department of Materials Science and Engineering

College of Engineering

Seoul National University

**A Study on the Correlations
between anti phase domain and luminescence
characteristics of alpha-Ga₂O₃ using deep-UV
Cathodoluminescence stage for Transmission
Electron Microscopy**

고 에너지 영역 투과전자현미경용 음극 형광
분석 시스템을 통한 alpha-Ga₂O₃ 기반
소자의 역상 도메인과 발광 특성과의
상관관계에 대한 연구

지도 교수 김 영 운

이 논문을 공학박사 학위논문으로 제출함
2023년 8월

서울대학교 대학원
재료공학부
이 용 희

이용희의 공학박사 학위论문을 인준함
2023년 8월

위 원 장	김 미 영	(인)
부위원장	김 영 운	(인)
위 원	장 호 원	(인)
위 원	양 철 웅	(인)
위 원	박 용 조	(인)

Abstract

In this thesis, we developed a deep UV Cathodoluminescence (CL) detection system which is compatible with ordinary TEM and used the system to study the effect of anti-phase domain(APD) of high crystalline alpha-Ga₂O₃ on luminescence characteristics.

First, we made the CL detection system to measure a deep UV range with TEM. In order to make a stage which can be used in TEM, the height of all components (mirror, lens, optical fiber, etc.) should be less than 3mm, which is the objective pole piece gap. Until now, commercialized lenses are made of BK7 and have a cut-off range of 350nm, so it is not possible for them to detect deep UV range. To solve the problem, we customize the lens with fused silica and extend the detection limit to 200nm. Then we optimize the system to detect the cathodoluminescence light with the minimum loss and maximum efficiency by using the following methods:

- (i) Aluminum, which has high reflectivity in a deep UV range, is used. Also, through electrolytic polishing, a perfect mirror shape was fabricated without deformation of the curvature calculated.
- (ii) The optical fibers with the lowest attenuation efficiency are used to minimize the loss.
- (iii) Grating and CCD, which could maximize quantum efficiency in the deep UV range, were used.
- (iv) To increase CL light emission and get more detailed spectral information,

a cooling system with liquid nitrogen is settled in the TEM specimen stage.

Second, we confirmed extra diffraction spots of high crystalline Ga_2O_3 originate in APD, through various analytical TEM techniques. In high crystallinity $\alpha\text{-Ga}_2\text{O}_3$ verified by XRD results, extra diffraction spots are observed in [110], [010] and [221] zones. However, no additional diffraction spots were observed in [001] zone. To find out the reason why there are no spots in zone [001], we expose focused electron beams on the region where extra diffraction spots are observed in dark field(DF) image of zone [221] and create a reference point at the same position in [001] zone. Various sizes of domains are observed near the reference point tilted to [001] zone in ADF images.

The correlation of these domains was analyzed through a Converged beam electron diffraction (CBED) technique. The CBED results show the presence of APD in the region where extra diffraction spots are observed. By atomic-resolution ADF image analysis, it is confirmed that the atomic resolution ADF image of the extra diffraction spot area is different from the in-phase domain (IPD) region, and bright Ga atoms with a constant period are observed. When overlapping IPD and APD atomic structures, Ga atoms are situated at the same position or the different position. In case of Ga atoms are overlapped at the same position, the proportion of Ga atoms increases and it makes Z-contrast in ADF image brighter. The periodicity of bright Ga atoms results in extra diffraction spots.

Third, we confirmed the origin of anti-phase domain of high crystalline Ga_2O_3 through various analytical techniques for TEM. The Al_2O_3 surface provides the template for further hetero-epitaxial growth, and the orientation of the nuclei of $\alpha\text{-Ga}_2\text{O}_3$ is determined by the initial seating positions. Ga atoms of APD are positioned on the hollow sites on equilateral oxygen triangles in the same way as the IPD. We used density functional theory (DFT) calculations to explore the interfacial stability of the Three possible atomic arrangements of inverted nuclei. Three possible configurations for DS2, DS3, and DS4 are considered since all 3 configurations are hollow sites centered on equilateral oxygen triangles. The simulation results confirmed that DS3 and DS4 were more stable than DS2, which is verified with the ADF Images of APD interface. In the case of nonstoichiometric interfaces containing oxygen vacancies, the IPD is still more stable than the APD. However, it should be noted that the energy difference between IPD and APD is reduced in the non-stoichiometric case. That is, the nucleation probability of APD can be enhanced if oxygen vacancies are involved in the nucleation process.

Finally, the effect of APD on luminescence characteristics was analyzed using the developed DUV TEM CL system. When checking the 2D luminescence image, the inside domain is brightly observed at a wavelength of 320nm, the domain boundary at a wavelength of 380-480nm, and a specific domain boundary at a wavelength of 350nm. A specific domain boundary,

bright at 350nm, is confirmed as an APD boundary by CBED. To find the luminescence characteristics difference between APD boundary and domain boundary, we did a DFT calculation for the atomic structure of pristine bulk and ADF boundary. Unlike pristine bulk, the defect state of 0.52eV is formed near the valance band in APD boundary. Although the intermediate defect state of 0.52eV does not exactly match to produce the single transition giving 350nm, which is 3.54eV, the DFT calculation result supports the association of 350nm peak and the defect state.

Therefore, the 350nm peak is believed to come from trap to trap transition related to the states formed induced by local strain, which is originated by different stacking sequences.

Keywords: Cathodoluminescence, Deep UV range, Transmission electron microscopy, Luminescence characteristics, alpha-Ga₂O₃, anti-phase domain, extra diffraction spots

Student ID: 2014-22526

Yong-Hee Lee

Table of Contents

<i>Abstract</i>	i
<i>Table of Contents</i>	v
<i>List of Figures</i>	vii
 Chapter 1. Introduction	1
1. 1. Background	1
1. 2. Scopes and organizations	6
1. 3. Bibliography	8
 Chapter 2. Development of a deep UV CL stage for transmission electron microscopy	10
2. 1. Introduction	10
2. 2. Experimental detail	14
2. 3. Results and discussions	22
2. 4. Summary	28
2. 5. Bibliography	29
 Chapter 3. Investigation of internal structure characteristic of high crystalline alpha-Ga ₂ O ₃	31

3. 1. Introduction	31
3. 2. Experimental detail	33
3. 3. Origin of extra diffraction spots	37
3. 4. Origin of anti-phase domain.....	42
3. 4. Summary	55
3. 5. Bibliography	56

Chapter 4. Luminescence properties related to anti-phase domain of high crystalline alpha-Ga ₂ O ₃	59
--------------------------------------------------------------------------------------------------------------------------------	----

4. 1. Introduction	59
4. 2. Experimental detail	61
4. 3. Results and discussions	66
4. 4. Summary	77
4. 5. Bibliography	78

Chapter 5. Conclusion	84
-----------------------------	----

Abstract (in Korean)	92
----------------------------	----

List of Figures

Figure. 1 **Various useful signals are emitted by the interaction between the electron beam and a sample.**

Figure. 2 (a) Schematic diagram of radiative transitions between the conduction band (E_C), the valence band (E_V), excitons (E_E), donor (E_D), and acceptor (E_A) levels in a semiconductor. (b) Schematic diagram of luminescence spectra.

Figure. 3 **Schematic diagram of acquisition process for cathodoluminescence in transmission electron microscope(TEM).**

Figure. 4 (a) Design of the light-collecting module of deep UV TEM CL stage and (b) Photo of the light-collecting module of deep UV TEM CL stage e

Figure. 5 **Reflectance of the candidate materials for parabolic mirror.**

Figure. 6 (a) Photo of aluminum mirror fabricated through mechanical polishing. (b) Photo of aluminum mirror fabricated through electrolytic polishing.

Figure. 7 (a) Transmittance of the candidate materials for focusing lens. (b) Transmittance of fused silica materials for focusing lens about deep UV CL stage.

Figure. 8 (a) Schematic diagram of transmittance process of incident light in spectrometer. (b) Quantum efficiency of candidate grating for

spectrometer. (c) Quantum efficiency of candidate charge-coupled device (CCD) for spectrometer.

Figure. 9 **Information of alpha-Ga₂O₃.** (a) Cross-sectional secondary electron (SE) image of as-grown alpha-Ga₂O₃. (b) XRD result of as-grown alpha-Ga₂O₃.

Figure. 10 (a) Schematic diagram of prepared TEM sample. (b) TEM image acquired in [001] zone axis.

Figure. 11 (a) TEM image of the area in which the CL characteristics were acquired. (b), (c) Luminescence spectra acquired from the red circle area in a during 2s and 10s, respectively.

Figure. 12 (a) Annular dark field (ADF) image of the area in which two-dimension luminescence maps were acquired. (b) Overlapped images of the 320 nm, 350 nm, and 380-480 nm wavelengths along with the ADF image using red, blue, and green, respectively. The corresponding CL maps are shown in (c)-(e) (the latter shows the wavelength range of the image). (f) Binning spectrum of 320 nm, 350 nm, and 380-480 nm.

Figure. 13 **Information of prepared TEM specimen.** (a) Schematic diagram of prepared TEM samples. (b), (c) ADF image of prepared TEM samples, [110], [001], respectively.

Figure. 14 **TEM images and electron diffraction from two observation directions from single-crystal alpha Ga₂O₃.** (a)-(d) are obtained in

[110] zone axis. (a) Bright-field image. (b) Electron diffraction image of (a). (c) Dark field image of $g_{\bar{1}10}$. (d) Dark field image of g_{002} . (e)-(g) are obtained in [010] zone axis. (e) Bright-field image. (f) Electron diffraction image of (e). (g) Dark field image of g_{002} . (h) [001] zone atomic model of alpha-Ga₂O₃.

Figure. 15 **TEM images and electron diffraction from two observation directions from single-crystal alpha Ga₂O₃**. (a)-(c) are obtained in [221] zone axis. (a) Bright-field image. (b) Electron diffraction image of (a). (c) Dark field image of $g_{1\bar{1}0}$. (d), (e) are obtained in [001] zone axis. (d) Bright-field image. (e) Electron diffraction image of (d). (f) Schematic diagram of three zones observed, [110], [221], and [001].

Figure. 16 **Confirmation of relative orientation relations using conversed beam electron diffraction(CBED)**. (a) ADF image was taken near the area where the extra diffraction spots were observed. (b) The CBED image indicated by numbers are shown in (b). (c) Atomic-resolution ADF image indicated by a green box in (a). (d) Atomic-resolution ADF image in lower magnification. (e) [001] zone atomic model of alpha-Ga₂O₃.

Figure. 17 **Origin of extra diffraction spots**. (a), (b) show atomic models of alpha-Ga₂O₃ viewed along [110] and [010], respectively. (c) is an atomic model of [110] and [010] crystal overlapped. (d), (e) are ADF

images observed from [110] and [010] zone, respectively, with FFT in the insets. (f) is the ADF images of the extra diffraction area (the inset is the FFT results). (g) is an enlarged ADF image of (f) with an atomic model overlaid.

Figure. 18 Formation mechanism of the anti-phase domains. (a) An atomic model of Al_2O_3 viewed from [001]. Perfect Al_2O_3 crystals have 3-fold bonding of Al-O with equilateral oxygen triangles with aluminum in the recessed position at the center of the oxygen triangle. The crystallographic orientation of the triangles may have 120-degree or 180-degree symmetry as indicated using semitransparent yellow and green, respectively. (b) The surface of the (001) Al_2O_3 has either an aluminum-terminated surface or the oxygen-terminated one. Pink oxygen represents the oxygen-terminated configuration and aluminum-terminated in brown, where aluminum is sky blue. When the aluminum-terminated layer of Al-O triangular bonding is removed, the next Al-O bonding reveals oxygen-terminated and inverted triangle geometry. Two possible configurations of inverted triangles, marked with dotted lines, are shown. The probability of forming the in-phase and anti-phase domains may be the same because both terminations have the same lateral distance between Al-O. Depending on the bonding direction (either “P” or “Q”) anti-phase domain may be formed. The bonding direction can be affected by

factors, such as the formation energy of Al-O, surface steps, and oxygen vacancies, which determine the orientation of the nuclei.

Figure. 19 **Observation of atom configuration of anti-phase domain boundary and in-phase domain boundary.** (a) ADF image of the in-phase domain $\text{Al}_2\text{O}_3/\text{Ga}_2\text{O}_3$ interface and the corresponding atomic model at $[110]$ zone. (b) An atomic model, viewed along $[001]$, of the interface marked by the red arrow in (a). A, B, and C are hollow sites centered on equilateral oxygen triangles, which are the same stacking sites as Al_2O_3 . X are hollow sites centered on isosceles oxygen triangles different from the stacking site as Al_2O_3 . (c) and (d) Atomic-resolution ADF Images and the corresponding atomic positions viewed at $[001]$ zone of anti-phase domain and in-phase domain boundary, respectively. The yellow arrows in (c) and (d) indicate the location of the high-contrast $\{110\}$ boundaries. When comparing the relative number density of gallium atoms from the arrow-marked plane and others, it does not give any fluctuations in the number of gallium atoms, regardless of the boundary type, anti-phase domain, or in-phase domain boundaries.

Figure. 20 **Atom configurations of possible configurations of Al-O stacking.**

Atomic models of Ga_2O_3 on Al_2O_3 viewed from $[110]$ ((a), (c), (e), and (g)) and viewed from $[001]$ ((b), (d), (f), and (h)). (a), (b) Atomic models of Ga_2O_3 stacking sequence same as Al_2O_3 (named as DS1

with A'B'(Al₂O₃)/(Ga₂O₃)CA-BC-AB stacking). (c),(d) DS2 atomic stacking of A'B'(Al₂O₃)/(Ga₂O₃)BA-CB-AC, (e),(f) DS3 atomic stacking of A'B'(Al₂O₃)/(Ga₂O₃)AC-BA-CB, and (g),(h) DS4 stacking of A'B'(Al₂O₃)/(Ga₂O₃)CB-AC-BA.

Figure. 21 **Origin of anti-phase domain.** (a) High-resolution ADF image of the typical Al₂O₃/Ga₂O₃ interface with the corresponding atomic model overlaid on [110] zone. (b) atomic model of the interface viewed along [001] in the regions marked with dotted-rectangular with orange in (a). (c) Calculated boundary formation energies based on the atomic model shown in Figure. 20. (d), (e) ADF image of domain stacking₃(DS3) of Al₂O₃/Ga₂O₃ interface and the corresponding atomic model at [110] zone, and an atomic model with DS1 and DS3 overlapped, respectively. (f), (g) ADF image of the DS4 of Al₂O₃/Ga₂O₃ interface and the corresponding atomic model at [110] zone with DS1 and DS4 overlapped.

Figure. 22 (a) Schematic diagram of prepared TEM samples. (b) ADF image of prepared TEM samples in [001].

Figure. 23 **Microstructure observed from [001] zone plan-view TEM.** (a) Schematic diagram of plan-view TEM (PTM) sampling area. (b) Low magnification brightfield TEM image of the area analyzed. Electron diffraction from the dotted circle is shown in the inset. (c) Annular darkfield (ADF) image showing boundaries, with (d) CBED

patterns with corresponding numbered regions marked in (c).

Figure. 24 (a) Low magnification HAADF image near the merged valley. (b) is an enlarged HAADF image to show the geometry of domain boundaries. Domains are developed along the growth direction as indicated in Figure. 23a and depending on the sampling region, two distinct regions, equiaxed and elongated boundaries, are visible.

Figure. 25 **Luminescence characteristics in Plan-view TEM.** (a), (b) Luminescence spectra obtained from the red circle area in Fig. 1(b) exposed electron beam for 2s and 10s, respectively. (c) ADF image used for CL analysis. (d)-(j) show a 2-dimensional mapping of a specific wavelength range, which is shown at the bottom of the figures.

Figure. 26 **Origin of boundary contrast.** (a) ADF image showing bright boundary contrast. (b),(c) are the gallium and oxygen electron energy loss spectroscopy (EELS) elemental mappings of the area shown in (a), respectively. (d) electron diffraction pattern at [001] zone, where the rotation of the domains is confirmed from the mosaic pattern of the diffraction spots as shown in the inset. (e)-(h) are ADF images with different ranges of collection angles. Collection angles are listed at the bottom of the figure.

Figure. 27 (a),(b) Low magnification two beam brightfield and dark field image of cross-section TEM with diffraction vectors of $g_{\bar{1}110}$, where

threading dislocations, marked with arrows, are visible. (c) High-resolution image of the interface to visualize the existence of the threading dislocations, and (d) the reconstructed image using $(\bar{3}30)$ after the filtering Fast Fourier-Transformed (FFT) image. (e) colorized image of FFT-reconstructed and ADF using red and green. Theoretical calculation gives one threading dislocation per 21.6 planes of $(\bar{3}30)$ but actual measurement reveals threading dislocations in every ~ 38 and ~ 44 $(\bar{3}30)$ planes, which means that the relief from the lattice mismatch was additionally relieved by the thin membrane substrate and mosaic domain structure formation.

Figure. 28 **Formation of in-plane rotation and the development of strain at the merging boundary.** (a) In the nucleation stage, a mosaic structure is developed to accommodate the lattice mismatch partially between the substrate and the film. (b) As the crystal grows in vertical and lateral directions, the crystal maintains the rotation and the lattice mismatch builds strain at the merging front.

Figure. 29 **Variations of Luminescence characteristics.** (a) Areal spectrum from inside domain, domain boundary, and APD boundary. (b) Gaussian deconvolution of each area spectrum of (a). It is fitted by seven Gaussian peaks corresponding to asymmetric shoulder and the relative peak heights reveal the difference in the energy states in 3 major areas of (a). (c) and (d) show the atomic model of $[001]$ and

[110] view, and the calculation results of the total density of states in the pristine bulk, respectively. (e) and (f) are for the anti-phase domain boundary of α -Ga₂O₃.

Chapter 1. Introduction

1. 1. Background

Accelerated electron beams interacting with materials emit various useful signals containing structural, chemical, and electrical information about the materials (Figure. 1).¹⁻³ When a solid is supplied with a certain type of energy it may emit photons or undergo a process called luminescence.

The luminescence process can be categorized according to the excitation source. Photoluminescence is due to photon excitation, chemiluminescence results from energy supplied by a chemical reaction, thermoluminescence arises from energy supplied by heating, electroluminescence is caused by excitation through the application of an electric field, and cathodoluminescence (CL) occurs due to excitation by an electron source. Thus, CL is the phenomenon of light emission resulting from electron bombardment on materials.

When the primary electrons excite the electrons in the material, the excited electrons release their excess energy as photons in accordance with their internal transitions. Therefore, the energy of the emitted

photons corresponds to the difference between the initial state E_i and the final state E_f of the excited electrons:

$$h\nu = \frac{hc}{\lambda} = E_f - E_i$$

There are several radiative transition modes between the conduction band, the valence band, and other extrinsic energy states in the bandgap (Figure. 2a). These radiative transition modes include conduction band to valence band transition, impurity-related transitions (conduction band to impurity, impurity to valence band, impurity to impurity, etc.), resulting in CL spectra composed of various peaks (figure. 2b).⁴⁻⁸

When CL spectroscopy is combined with electron microscopy, the optical properties of materials can be analyzed alongside microscope images. As a result, electron microscopy-CL is a research field that utilizes luminescence spectra to understand and characterize material properties on a microscopic level.

Currently, there are two basic types of CL analysis systems: one based on electron microscopes and the other on scanning electron microscopes (SEMs) or scanning transmission electron microscopes (STEMs). The SEM-CL technique can obtain abundant signals and analyze physical properties related to defects near the surface of a

material.⁹⁻¹² However, it has poor resolution due to the pear cascade. The STEM-CL technique, on the other hand, has a small interaction volume due to high acceleration voltage and thin specimen thickness (<100 nm). While the generated signal is weaker compared to SEM-CL, STEM-CL offers very high resolution due to its small interaction volume.^{13,14}

Therefore, the STEM-CL technique enables the analysis of the relationship between the optical properties and internal structural properties of nanosized materials.¹⁴⁻¹⁷

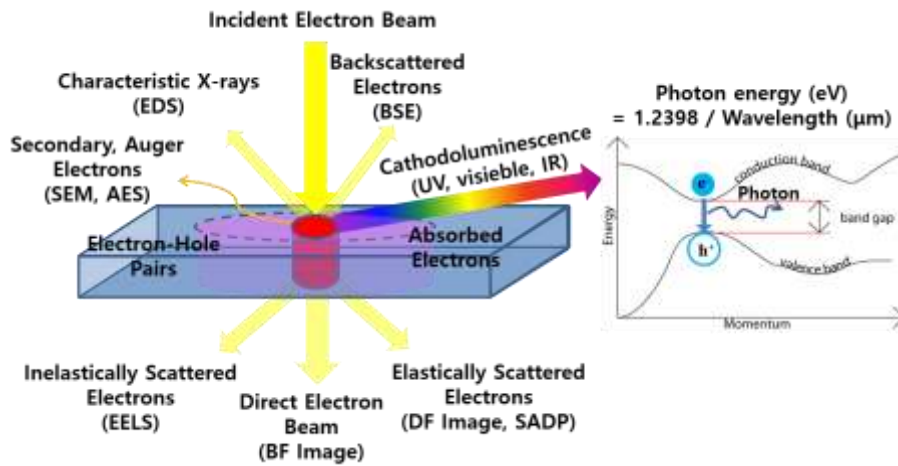


Figure. 1 Various useful signals are emitted by the interaction between the electron beam and a sample.

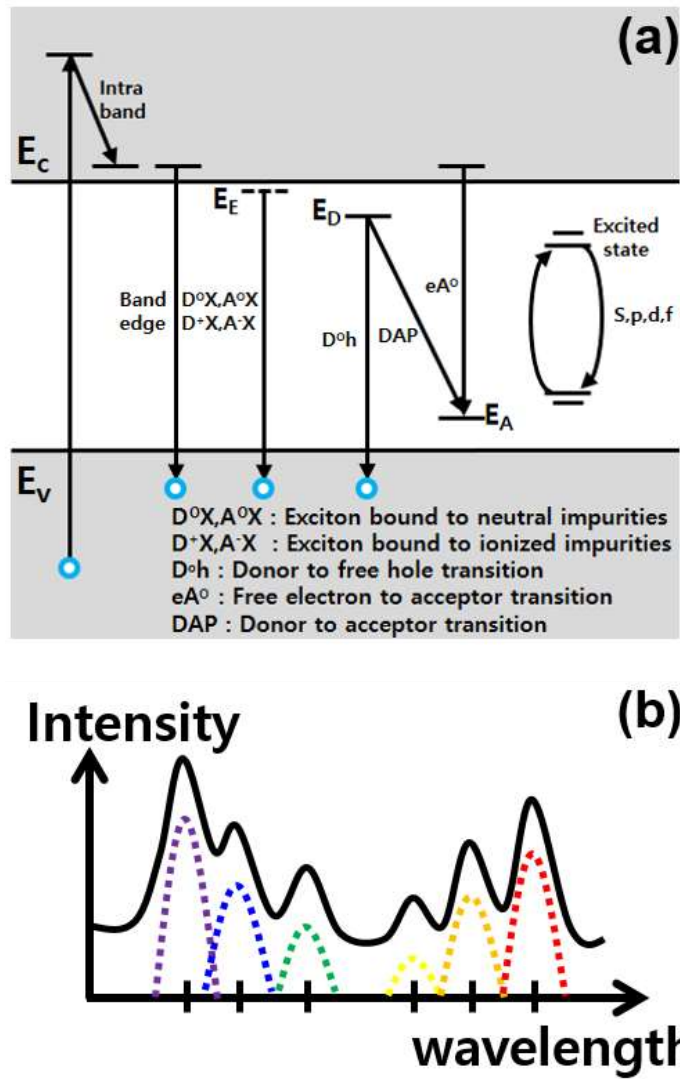


Figure. 2 (a) Schematic diagram of radiative transitions between the conduction band (E_c), the valence band (E_v), excitons (E_E), donor (E_D), and acceptor (E_A) levels in a semiconductor. (b) Schematic diagram of luminescence spectra.

1. 2. Scopes and organizations

This thesis consists of 5 chapters. Chapter 1 presented the introduction as stated above.

Chapter 2 covers the fabrication of a Deep UV(DUV) TEM CL Stage. This chapter presents the key feature of the DUV CL stage. The mirror surface of aluminum was formed through electro-polishing without deformation of calculated curvature. And detection limit was expanded from 350nm to 200nm by using a custom-made fused silica lens. And DUV range(<350nm) efficiency can be maximized by optimized optical fiber and detector. Performance and applicability of the DUV CL stage was successfully demonstrated by Ga₂O₃

Chapter 3 presents the origin of extra diffraction spots related Anti-phase domain for high-crystalline alpha Ga₂O₃. Origin of extra diffraction spots were verified by various techniques (BF and DF image, CBED pattern, atomic resolution ADF image, and atomic model). Origin of anti-phase domain was verified by DFT calculation, atomic resolution ADF image, and an atomic model.

Chapter 4 presents Luminescence properties related anti-phase domain for high crystalline alpha-Ga₂O₃. Luminescence characteristics were acquired by DUV CL stage for TEM. The relationship between luminescence characteristics and internal structure was verified by CBED pattern, atomic

resolution ADF image, atomic model, and DFT calculation. The atomic model of anti-phase domain boundary for DFT calculation was confirmed through atomic configuration analysis.

At the conclusion, chapter 5 summarized this thesis.

1. 3. Bibliography

- ¹ Arnold Gucsik, *Cathodoluminescence and its application in the planetary sciences*. (Springer, Berlin, 2009), pp.xii.
- ² B. G. Yacobi and D. B. Holt, *Cathodoluminescence microscopy of inorganic solids*. (Plenum Press, New York, 1990), pp.ix.
- ³ V. I. Petrov, *Usp Fiz Nauk* **166** (8), 859 (1996).
- ⁴ R. Mitdank, A. Sveshnikova, E. Schulze, G. Oelgart, and F. K. Reinhart, *Semicond Sci Tech* **10** (6), 835 (1995).
- ⁵ Gerald Martin William and Birmingham University of, *The study of electronic materials for light emitting devices using scanning cathodoluminescence electron microscopy*. (University of Birmingham, Birmingham, 2002), p.1 v. (various pagings) : ill.
- ⁶ E. M. Hörl, *Scanning electron microscopy of biological material using cathodoluminescence*.
- ⁷ Jens Götze, *Cathodoluminescence microscopy and spectroscopy in applied mineralogy*. (Technische Universität Bergakademie Freiberg, Freiberg, 2000), pp.128p. : ill. (some col.).
- ⁸ Nicholas C. Burton, *Characterisation of strain and microstructure variation in synthetic diamond by electron microscopy and cathodoluminescence*. (University of Bristol, 1995).

- ⁹ D. B. Darby and G. R. Booker, *J Mater Sci* **12** (9), 1827 (1977).
- ¹⁰ G. Koschek, *J Microsc-Oxford* **171**, 223 (1993).
- ¹¹ J. Evans, A. J. C. Hogg, M. S. Hopkins, and R. J. Howarth, *J Sediment Res A* **64** (2), 334 (1994).
- ¹² M. F. Hamers and M. R. Drury, *Meteorit Planet Sci* **46** (12), 1814 (2011).
- ¹³ N. Yamamoto, *Microscopy-Jpn* **65** (4), 282 (2016).
- ¹⁴ P. Sutter, C. Argyropoulos, and E. Sutter, *Nano Lett* **18** (7), 4576 (2018).
- ¹⁵ E. Nogales, B. Mendez, and J. Piqueras, *Appl Phys Lett* **86** (11) (2005).
- ¹⁶ G. Schmidt, P. Veit, C. Berger, F. Bertram, A. Dadgar, A. Strittmatter, and J. Christen, *Jpn J Appl Phys* **55** (5) (2016).
- ¹⁷ Jiannong Wang, (1990).

Chapter 2. Development of a Deep UV CL Stage for transmission electron microscopy

2. 1. Introduction

Cathodoluminescence (CL) is an optical and electrical phenomenon that arises from interactions between accelerated electrons and materials.¹⁻³ CL analysis is typically performed using an accelerated electron beam as the excitation source. Electromagnetic lenses can focus electrons into a sub-nanometer-sized spot. By scanning the focused electron beam, CL spectra can be collected at each point of the scanned region, and the microstructure of that region can be observed.⁴⁻⁶ To collect the emitted light from the sample, equipment is needed to set up light-collecting optical components such as mirrors, lenses, and light guides, as well as a spectrometer to analyze the collected light.

Figure 3 shows a schematic diagram of the emitted light flow and an image of the TEM-CL stage set up in 2100F(JEOL). The electron beam scan position is adjusted through the electron beam control unit, and the spectra of the position where the electron beam is irradiated are obtained. A 2D luminescence map is formed using the obtained spectra. The internal structure and luminescence characteristics can be analyzed through the annular dark field image at the same position as the 2D luminescence map.^{7,8} To be compatible

with both SEM and TEM, all parts used in the CL stage must have a size of 3 mm or less, as the size of the pole piece gap in TEM is smaller than 3 mm.

Unlike SEM-CL, TEM-CL techniques have a very small interaction volume due to their high acceleration voltage and thin specimen thickness of 100 nm or less.^{4,9-12} Consequently, TEM-CL techniques have a weaker intensity than SEM-CL techniques. Furthermore, in high-energy UV regions below 300 nm, the spectral intensity rapidly attenuates due to absorption from the lens located at the CL system, optical fiber, and light collection stages of the CCD camera. Therefore, to acquire high-energy UV regions below 300 nm, the TEM-CL stage requires radiative recombination to be maximized and optimization to reduce attenuation.

When developing a TEM-CL stage, it first needs to be designed to create a cryogenic environment. CL intensity increases as the temperature is lowered because radiative recombination becomes more favored compared to competing non-radiative recombination. CL measurements can be performed at cryogenic temperatures using liquid nitrogen as a cryogen. CL spectra can be sharpened into lines and series of lines corresponding to transitions between well-defined energy levels due to a reduction in thermal excitation of carriers. Secondly, optical components and detectors should be selected to minimize the decrease in intensity. Lastly, the lens should be designed with a material suitable for the wavelength region to be detected, as the cut-off range varies depending

on the lens material.

In this study, we developed a DUV CL detection system compatible with an ordinary TEM, which is a light-collectible TEM specimen stage. We carefully arranged the optical components such as mirrors, lenses, and optical fibers within the TEM specimen stage. To expand the detection limit, we chose UV-grade fused silica lenses. Electrolytic polishing was used to form a perfect mirror without burrs. Furthermore, we combined a specimen cooling system with the light-collectible TEM specimen stage.

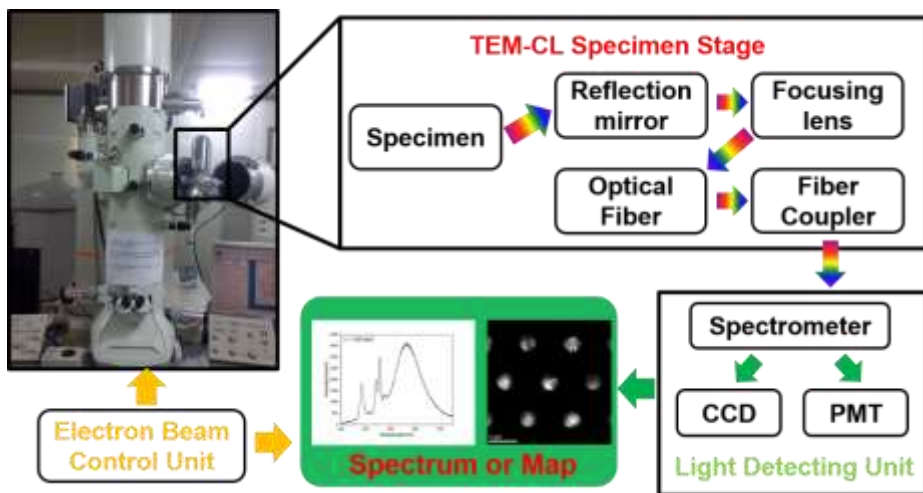


Figure. 3 Schematic diagram of acquisition process for cathodoluminescence in transmission electron microscope(TEM).

2. 2. Experimental detail

The design of the DUV CL stage is shown in Figure 4a, while the produced stage is depicted in Figure 4b. To detect a high-energy UV region below 300nm, a mirror capable of reflecting light in the high-energy UV region and a lens capable of focusing the reflected light into the fiber should be selected. The reflectance of each material is shown in Figure 5.

Au is a material optimized for the infrared region because it has a reflectivity of 99% or more in a wavelength region of 700nm or more. Ag can reflect up to a wavelength of 400nm compared to Au, but it is not suitable for the deep UV region because it has a reflectivity of 30% or less in an area of 300nm or less. In contrast, aluminum is a material optimized for DUV wavelengths because it has a reflectivity of more than 90 percent up to 200nm.

Aluminum is a very soft material and has excellent processability, but it is soft, so burrs are easily formed by processing tools. Figure 6a shows that mechanical polishing of aluminum does not form a perfect mirror surface, and burrs remain. If further polishing is performed to eliminate these burrs, the calculated curvature is deformed, preventing the production of a mirror with maximum efficiency. An electrolytic polishing method was adopted to produce a mirror with maximum efficiency without deformation of curvature. Figure 6b shows a mirror fabricated through electrolytic polishing, confirming that a

perfect mirror is formed without deformation of the calculated curvature.

Figure 7a presents a table that shows the transmission characteristics of candidate mirror materials, revealing that the transmittance curve for each material is different. The most critical point for use in the TEM-CL stage is that the size of the lens should be less than 3mm. Among the materials in Figure 7a, BK7 is the only lens commercially available in a size smaller than 3mm. Therefore, the previously produced TEM-CL stage has a detection limit of 350nm, and the deep UV range of 350nm or less could not be measured. As shown in Figure 7b, fused silica material should be used to measure the DUV wavelength region. With fused silica, the detection range can be extended up to 200nm. Since the fused silica lens was not manufactured in a size smaller than 3mm, a DUV TEM-CL stage was fabricated using a customized 3mm fused silica lens. The custom-made lens is shown in Figure 4b.

In a high-energy UV region below 300nm, the spectral intensity attenuates rapidly due to absorption from the lens located at the CL system, optical fiber, and light collection stages of the CCD camera. Optimization of the grating and CCD is required to minimize light loss.

Figure 8a is a schematic diagram illustrating a process in which light incident through optical fibers goes to a detector. Light incident through the optical fiber decomposes through the grating and then enters each CCD. To minimize loss, an optimized system was constructed by selecting a 300nm

grating and a UVB-type CCD. The efficiency of the grating and CCD is shown in Figures 9b and 9c.

The fabricated DUV TEM-CL stage was verified using Alpha Ga_2O_3 , which is reported to have an energy bandgap of 4.7 to 5.6 eV.

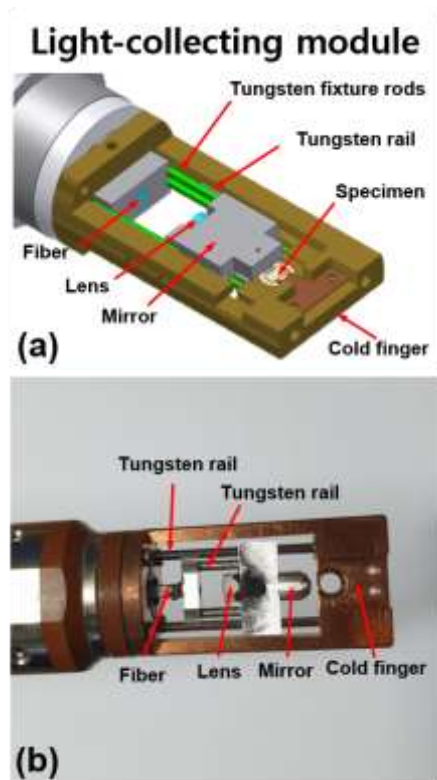


Figure. 4 (a) Design of the light-collecting module of deep UV TEM CL stage and (b) Photo of the light-collecting module of deep UV TEM CL stage.

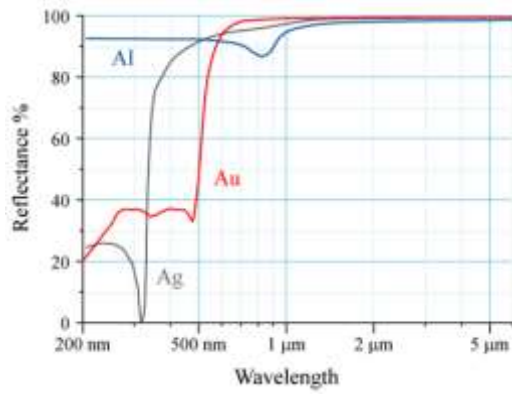


Figure. 5 Reflectance of the candidate materials for parabolic mirror.

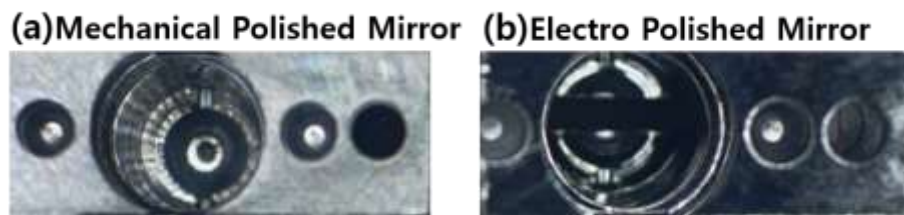


Figure. 6 (a) Photo of aluminum mirror fabricated through mechanical polishing. (b) photo of aluminum mirror fabricated through electrolytic polishing.

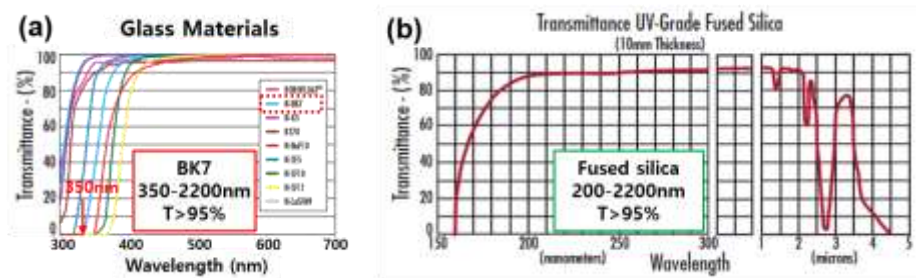


Figure. 7 (a) Transmittance of the candidate materials for focusing lens. (b) Transmittance of fused silica materials for focusing lens about deep UV CL stage.

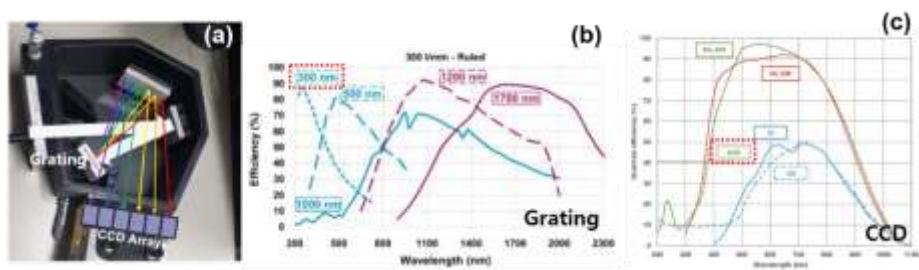


Figure. 8 **Schematic diagram of transmittance process of incident light in spectrometer.** (b) Quantum efficiency of candidate grating for spectrometer. (c) Quantum efficiency of candidate charge-coupled device(CCD) for spectrometer.

2. 3. Results and discussions

Figure 9a displays the SE image of alpha gallium oxide, and Figure 9b shows the XRD result. α -Ga₂O₃ thin films were grown on the tops of the Al₂O₃ bridges, which were used as templates for the growth. The XRD results confirm the existence of single-crystal alpha-Ga₂O₃ with high crystallinity. A TEM sample was prepared as a plan view TEM to measure only the luminescence characteristics of gallium oxide without Al₂O₃. Figure 10a is a schematic diagram of the specimen produced, and Figure 10b is the [001] zone TEM image of the specimen.

In a high-energy UV region under 300nm, the spectral intensity attenuates rapidly due to absorption from the optical parts. In this test, it was possible to obtain a UV range peak of ~223nm (5.56 eV) - as shown in Figure 11c - when the spectral collection time was increased to 10 seconds. Since the band edge is reported to have an energy of 4.9-5.6 eV (263nm-217nm) for alpha Ga₂O₃, the 223nm peak is considered to be a near band edge transition.¹³⁻¹⁶

It was verified that the system produced through the band edge transition peak of 223nm can be detected up to 200nm, although the electron beam was exposed for 10 seconds. It was tested whether a two-dimensional luminescence map could be acquired using the fabricated deep UV CL system, and the results are shown in Figure 12.

Figure 12a shows an ADF image of an area acquired to investigate the area-specific luminescence characteristics. Figure 12c-e displays spectrum images (SI) that have been extracted with specific wavelengths, showing local luminescence characteristic differences. Figure 12b presents the overlapped images of the 320nm, 350nm, and 380-480nm wavelengths along with the ADF image using red, blue, and green, respectively.

A strong 320nm peak is observed inside the domain, while 380-480nm peaks are more strongly detected at the domain boundary. One of the boundaries reveals singular luminescence characteristics of 350nm, and it appears purple in Figure 12b. Figure 12f shows the corresponding spectra. Through Figure 12, it is confirmed that the deep UV TEM CL system can acquire a two-dimensional luminescence map even below 350nm.

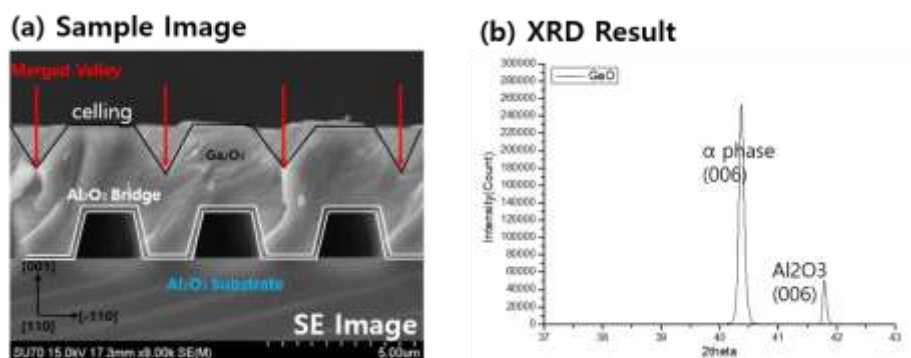
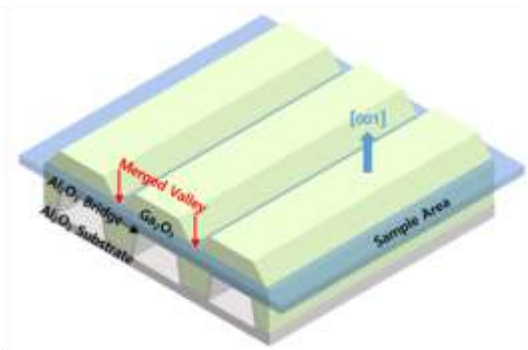


Figure. 9 (a) Cross-sectional secondary electron(SE) image of as-grown alpha- Ga_2O_3 . (b) XRD result of as-grown alpha- Ga_2O_3 .

(a) Schematic diagram



(b) Sample Image

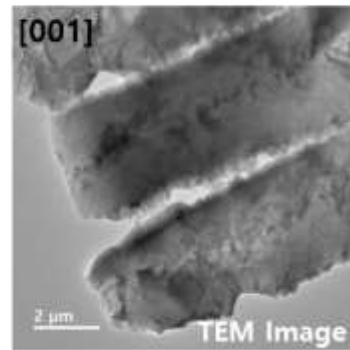


Figure. 10 (a) Schematic diagram of prepared TEM sample. (b) TEM image acquired in $[001]$ zone axis.

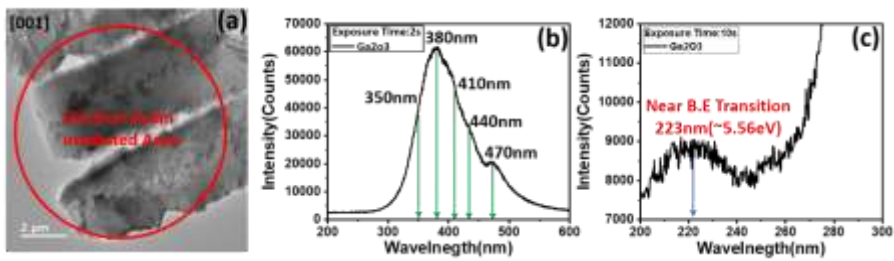


Figure. 11 (a) TEM image of the area in which the CL characteristics were acquired. (b), (c) Luminescence spectra acquired from the red circle area in a during 2s and 10s, respectively.

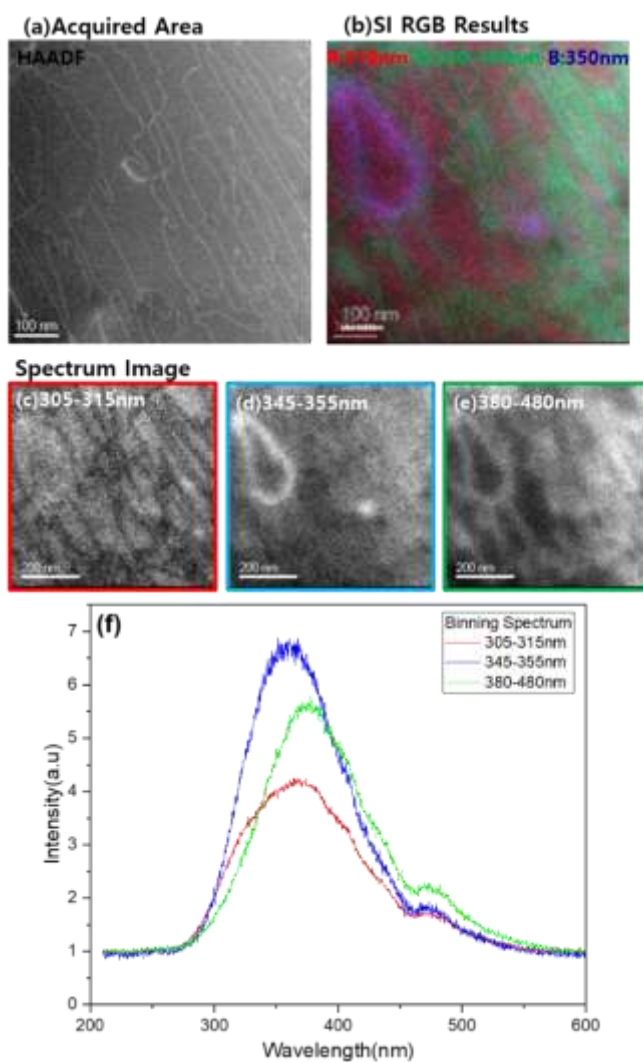


Figure. 12 (a) Annular dark field(ADF) image of the area in which two-dimension luminescence maps were acquired. (b) Overlapped images of the 320 nm, 350 nm , and 380-480 nm wavelengths along with the ADF image using red, blue and green, respectively. The corresponding CL maps are shown in (c)-(e) (the latter shows the wavelength range of the image). (f) Binning spectrum of 320 nm, 350 nm and 380-480 nm.

2. 4. Summary

In order to collect and detect high-energy UV region below 300 nm from the TEM sample, a DUV TEM-CL stage was developed. By optimized design and arrangement of optical components on the TEM stage, detect high-energy UV region CL lights are successfully detected by a spectrometer. And to increase the CL intensity and get more detailed spectral information from the CL signals, we combined the liquid nitrogen cooling system with the light collectible TEM stage specimen.

2. 5. Bibliography

- ¹ Jens Götze, *Cathodoluminescence microscopy and spectroscopy in applied mineralogy*. (Technische Universität Bergakademie Freiberg, Freiberg, 2000), pp.128p. : ill. (some col.).
- ² Arnold Gucsik, *Cathodoluminescence and its application in the planetary sciences*. (Springer, Berlin, 2009), pp.xii.
- ³ V. I. Petrov, *Usp Fiz Nauk* **166** (8), 859 (1996).
- ⁴ N. Yamamoto, *Microscopy-Jpn* **65** (4), 282 (2016).
- ⁵ Gerald Martin William and Birmingham University of, *The study of electronic materials for light emitting devices using scanning cathodoluminescence electron microscopy*. (University of Birmingham, Birmingham, 2002), p.1 v. (various pagings) : ill.
- ⁶ E. M. Hörl, *Scanning electron microscopy of biological material using cathodoluminescence*.
- ⁷ S. J. Pennycook, *Annu Rev Mater Sci* **22**, 171 (1992).
- ⁸ N. D. Browning, M. F. Chisholm, and S. J. Pennycook, *Nature* **366** (6451), 143 (1993).
- ⁹ E. Nogales, B. Mendez, and J. Piqueras, *Appl Phys Lett* **86** (11) (2005).
- ¹⁰ P. Sutter, C. Argyropoulos, and E. Sutter, *Nano Lett* **18** (7), 4576 (2018).
- ¹¹ G. Schmidt, P. Veit, C. Berger, F. Bertram, A. Dadgar, A.

- Strittmatter, and J. Christen, *Jpn J Appl Phys* **55** (5) (2016).
- ¹² Jiannong Wang, (1990).
- ¹³ A. Segura, L. Artus, R. Cusco, R. Goldhahn, and M. Feneberg, *Phy Rev Mater* **1** (2) (2017).
- ¹⁴ N. S. Jamwal and A. Kiani, *Nanomaterials–Basel* **12** (12) (2022).
- ¹⁵ S. D. Lee, Y. Ito, K. Kaneko, and S. Fujita, *Jpn J Appl Phys* **54** (3) (2015).
- ¹⁶ A. K. Mondal, M. A. Mohamed, L. K. Ping, M. F. Mohamad Taib, M. H. Samat, M. A. S. Mohammad Haniff, and R. Bahru, *Materials (Basel)* **14** (3) (2021).

Chapter 3. Investigation of internal structure characteristic of high crystalline α -Ga₂O₃

3. 1. Introduction

Ga₂O₃ has unique characteristics of wide bandgap and high breakdown voltage, making it suitable for many applications in transparent conductive layers, power devices, and deep UV optical sensors.¹⁻⁵ Ga₂O₃ has been reported to have six crystal structures of α , β , γ , ϵ , δ , and κ , where the β -phase is known to be the most stable phase.^{6,7}

The research on β -Ga₂O₃ represented the mainstream direction in the early stage of Ga-O research, as it was possible to make bulk substrates using the conventional fabrication methods of the floating zone and the Czochralski method, therefore making it possible to grow homo-epitaxy thin films with high crystallinity.⁸⁻¹⁴ Growing a homoepitaxial Ga₂O₃ thin film is an expansive process, and growing it on an inexpensive sapphire substrate would be a better choice for the practical production of Ga₂O₃ devices.^{3,15-18}

In this thesis, a high-quality α -Ga₂O₃ thin film was grown using a thin membrane substrate while taking advantage of the similar crystal

structures of α -Ga₂O₃ and Al₂O₃. The physical properties and defect structures of high-quality α -Ga₂O₃ films need to be identified, as these can be essential for developing high-performance devices.

In this chapter, we report on the formation of an anti-phase domain (APD) when α -Ga₂O₃ is grown on the thin membrane alumina oxide substrate, which originated from the symmetry of the substrate and origin of extra diffraction spots.

3. 2. Experimental detail

Al_2O_3 nanomembranes were prepared on a 2-inch sapphire wafer in tent-shaped channels [110]. Stripe patterns with a rectangle thin-membrane of photoresist (PR) in cross-sections with a height and width of $2\mu\text{m}$ were prepared using photolithography on the c-plane sapphire substrate. An amorphous alumina layer of 60nm was deposited on PR-patterned sapphire substrates using atomic layer deposition and then crystallized by solid phase epitaxy.¹⁹⁻²¹

Finally, $\alpha\text{-Ga}_2\text{O}_3$ thin films were grown on a stripe-patterned sapphire nanomembrane substrate using mist CVD. Figure. 9a is cross-sectional secondary electron microscopy(SEM) image and Figure. 9b is an X-ray diffraction(XRD) result of as-grown alpha Ga_2O_3 . The XRD results confirm the existence of single-crystal alpha- Ga_2O_3 with high crystallinity.^{15,16}

TEM specimens were prepared by mechanical grinding/polishing, after which they were ion-polished using a 3keV beam using a commercially available ion polishing system (Gatan 691). Two different plane standard samples—[110] and [221]—were prepared to investigate the 3-dimensional microstructure in transmission electron

microscopy (TEM). The samples as well as the viewing planes are schematically presented in Figure. 14, along with the corresponding annular dark field (ADF) zone images.

Conventional TEM Images, electron diffraction (ED), and convergent beam electron diffraction (CBED) were taken using a JEM-2100F TEM (Japan Electron Optics Limited) operated at 200kV. Atomic-resolution ADF and images were obtained using a Themis-Z Cs-corrected TEM (Thermo-Fischer) operated at 200kV.

The density functional theory (DFT) calculations perform the Vienna ab initio simulation package (VASP). A projector-augmented wave (PAW) method is used for interactions between the valence electrons and the ionic cores. The generalized gradient approximation (GGA) in the Perdew-Burke-Emzerhof (PBE) formulation was used for exchange-correlation function. The electron wave function expands a base set of plane waves with a kinetic energy cut off 500 eV.

The redefined $\text{Ga}_2\text{O}_3/\text{Al}_2\text{O}_3$ boundary models with 60 atoms, with an $8 \times 8 \times 2$ gamma-centered k-point set, were fully relaxed until all energies were smaller than 0.01 eV/Å (by fully relaxing the atomic positions and lattice parameter). With a $4 \times 6 \times 2$ gamma-centered k-point set, the redefined anti-phase domain boundary models were fully relaxed

with 240 atoms until they were smaller than 0.01 eV/Å (by fully relaxing only the atomic positions with fixed experimental lattice parameters). The convergence threshold for the self-consistent field (SCF) iteration was set at 10^{-7} eV. Spin-constrained calculations were conducted for all models.

The formation energy was calculated based on the following formula.²²

$$E^f(q, E_F) = E_{tot}(q) - \sum_i n_i \mu_i + qE_V + qE_F$$

Where E^f is the formation energy, E_{tot} is the total energy of the defect cell, n_i is the number of i atoms in the supercell, μ_i is the corresponding chemical potential, q is the charge state of the defect, E_V is the energy of the valence-band maximum in bulk, and E_F is the Fermi level defined to be zero at the bulk valence-band maximum.

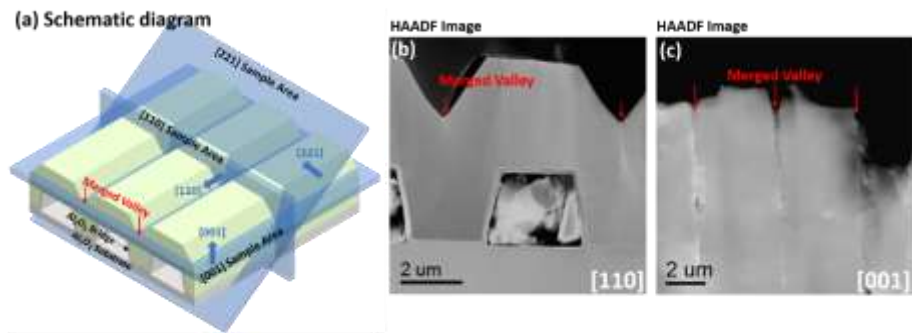


Figure. 13 **Information on prepared TEM specimen.** (a) Schematic diagram of prepared TEM samples. (b), (c) ADF image of prepared TEM samples, $[110]$, $[001]$, respectively.

3. 3. Origin of extra diffraction spots

Figure. 15a is a brightfield (BF) image taken along the $[110]$ zone axis, with the corresponding electron diffraction (ED) in Figure. 15b. Additional extra diffraction points are observed in Figure. 15b and marked with yellow circles which are not supposed to appear in $[110]$ zone single-crystal diffraction from perfect α -Ga₂O₃.

When observing the darkfield (DF) image, using one of the diffraction spots inside the yellow circles in Figure. 15b, the thin plates are confirmed as sources of additional diffraction spots, the shape of the plates is shown in Figure. 15c. The inter-planar spacings of the extra diffraction spots were found to be 0.437 nm along the direction $[\bar{3}30]$ and 0.678 nm in the $[006]$ direction.

Fig. 15c shows DF images of $g_{\bar{1}10}$, which is the first extra diffraction spot along $[\bar{3}30]$. The plate-shaped crystal, having widths of 10-20 nm from $[110]$ viewing direction and giving rise to extra diffraction spots, stems from the initial growth stage and maintains its widths during further growth. This is confirmed once again through Figure. 15e,f and g, the result of $[010]$ zone.

A plan-view TEM (PTM) sample was prepared to observe along $[221]$ to construct a 3-dimensional pattern of the plate-shaped crystal, and this direction was chosen for two reasons: first, it allows for observation along the parallel direction of the plate-like feature to the growth direction, and second,

it is possible to tilt the foil to reach the $[001]$ zone, which is the average direction of $[110]$, additional viewing direction to construct the 3-dimensional shape of the plates observed along $[110]$. An electron beam is focused onto the sample and produces holes to be used as reference points to ensure that the images are obtained from the same area in the $[001]$ zone. Red arrows indicate holes used as references in Figure. 15a, c, and d.

Figure. 15af is a BF image taken in the $[221]$ zone with the corresponding ED in Figure. 15b. As in Figure. 15b, the extra diffraction spots are marked with a yellow circle. The extra diffraction spots in the $[221]$ zone have an inter-planar spacing of 0.365 nm and 0.437 nm along $[0\bar{3}6]$ and $[\bar{3}30]$, respectively. The periodicity in the $[221]$ zone coincides with the $[\bar{3}30]$ periodicity in the $[110]$ zone, zone, which implies that the inter-planar spacing is from the same origin.

Figure. 15c is the $g_{\bar{1}10}$ DF image, obtained using the first extra diffraction spot along the $[\bar{3}30]$ direction. The DF reveals islands of a domain, slightly elongated in the $[110]$ direction, which concludes that the region-delivering extra diffraction has a columnar shape.

Figure. 15d and e are the BF images and the $[001]$ zone ED, respectively, taken by tilting 36 degrees from the $[221]$ zone, where the marking holes were positioned to confirm all the observations were made from the same area. Interestingly, as shown in Figure. 15b, no extra diffraction spots can be

observed when viewed in the [001] zone, which means that the Ga₂O₃ film maintains a hexagonal structure along the [001] axis.

The existence and disappearance of the extra diffraction spots from two different viewing directions [221] and [001] imply the existence of an anisotropic orientation characteristic of [221] with different domains while maintaining the hexagonal structure [001].

Convergent beam electron diffractions (CBED) were taken to determine the crystallographic difference between the domains, and the results are shown in Figure. 16b. Six different positions—marked with corresponding numbers in Figure. 16a and b—were selected, and the 3-dimensional diffraction from the Higher-Order Laue Zones (HOLZ) patterns is compared. All domains reveal 3-fold symmetry, but #3 reveals a 180-degree inversion (as in a 60-degree rotation) compared to the surrounding domains.²³⁻²⁵ Figure. 16c shows an atomic-resolution ADF image of the area of the green box in Figure. 16a, obtained from Cs-Corrected TEM, with APD boundaries showing high contrast in ADF.^{26,27} No distinct difference was observed except for more significant variability in atomic-resolution ADF. The lower magnification image reveals domain boundaries with facets on {110} planes, as shown in Figure. 16d, whose planes are schematically represented in Figure. 16e. The contrast is believed to come to the interface arising from rotated domain boundaries; this will be detailed in a later section.²⁸⁻³⁰

The #3 domain, which is anti-phase domain, provided the origin of extra diffraction spots when viewed from the [010] or [110] directions, as shown schematically in Figure. 17. The correlation between APD and IPD is investigated using the atomic resolution ADF Image and the Ga_2O_3 atomic model. Figure. 17a and b are atomic models of Alpha- Ga_2O_3 viewed from the [110] and [010] directions, respectively. The gallium planes are tilted by 60 degrees from the [001] direction in two different directions, which are seen in the ADF images in the [110] and [010] zone, as shown in Figure. 17d and e, respectively. Insets depict the ADF's Fast Fourier transformations (FFT) to show the relative positions of the diffraction spots. The FFT also has no extra spot observed.

Figure. 17c shows an atomic model of overlapped domains of [110] - and [010]-orientated crystals, while Figure. 17f shows an ADF image taken from a region of extra diffraction spots on [110] TEM sample. The projection view of the atomic model of the overlapping crystal and the enlarged ADF in Figure. 17g, including the inter-planar spacing of the planes—0.437 nm and 0.678 nm—exactly match the gallium positions.

When the domains of [110] and [010] zones are overlapped along the electron beam direction, the perfectly aligned Ga atoms form a new periodic gap and form extra diffraction spots, as can be seen in the inset of Figure. 17f. Based on the atomic models, CBED, and observed ADF image, it can be

concluded that the extra diffraction spots in Figure. 14b, g and figure. 15b originated from APD.

3. 4. Origin of anti-phase domain

Anti-phase domain (APD)s are believed to form in the nucleation stage of thin films. The Al_2O_3 surface provides a template for further hetero-epitaxial growth, and the initial nucleation conditions determine the orientation of the nuclei of $\alpha\text{-Ga}_2\text{O}_3$. The Ga atoms of Ga_2O_3 and Al atoms of Al_2O_3 are placed in hollow sites centered on equilateral oxygen triangles. The hexagonal arrangement of (001) Al_2O_3 leaves an equal probability of 120-degree rotation and 180-degree rotated nucleation templates. (Figure. 18) The distance between Ga atoms, located on the hollow sites on equilateral oxygen triangles, is similar to the one in the in-phase domain (IPD). The distance between Ga atoms is verified in high-resolution ADF in Figure. 16c from APD boundary, APD, and IPD (Figure. 19, explains the result of the Ga-Ga atomic distance measurement, where Figure. 20c-h shows the three possible atomic arrangements of inverted nuclei.). In addition to the observation that the distance between Ga atoms sustained throughout the crystal, no abnormal contrast was observed in between Ga column positions, which indicates that the atomic positions of Ga did not change regardless of the areas of IPD, APD, and domain boundaries.

It was found that there can be 3 possible stackings while maintaining Ga atom positions during the growth of Ga_2O_3 . Al-O bonding triangles in (001) Al_2O_3 layer reveal 3 distinct configurations in the sequence of C'A'-B'C'-A'B' stacking of Al_2O_3 when the crystal is viewed along [110], as shown in Figure.

21a, where the atomic model is overlaid on the ADF image at the interface, with the enlarged atomic model in the inset. We investigate the initial occupation sites of Ga for the Ga_2O_3 growth. The first nucleation of layers of $\alpha\text{-Ga}_2\text{O}_3$ will be one of A, B, and C, which depends on the exposed layer of A', B', and C'.

Assuming that the nucleation set the atomic positions and there is no change in the Ga Position in the further growth, we used density functional theory (DFT) calculations to investigate the interfacial stability of the nucleus models. 4 different configurations of stacking at the interface, domain stacking (DS)1- $\text{A}'\text{B}'(\text{Al}_2\text{O}_3)/(\text{Ga}_2\text{O}_3)\text{CA-BC-AB}$ stacking - maintain the stacking sequence of Al_2O_3 (Figure. 20a-b), DS2 - $\text{A}'\text{B}'(\text{Al}_2\text{O}_3)/(\text{Ga}_2\text{O}_3)\text{BA-CB-AC}$ stacking – (Figure. 20c-d), DS3 - $\text{A}'\text{B}'(\text{Al}_2\text{O}_3)/(\text{Ga}_2\text{O}_3)\text{AC-BA-CB}$ stacking – (Figure. 20e-f), and DS4 - $\text{A}'\text{B}'(\text{Al}_2\text{O}_3)/(\text{Ga}_2\text{O}_3)\text{CB-AC-BA}$ stacking – (Figure. 20g-h), are assumed because all three configurations have configurations of hollow metallic sites centered on equilateral oxygen triangles. Figure. 21c shows the calculation results of the interfacial formation energy of the four stacking models as a function of the Fermi level; Depending on the Fermi level, different charge states at the interface can transit to the ground states.²² In order to compare the energy states with different oxygen bonding configurations, two variations are adopted. An atomic model of fully bonded metal ions with full 3 oxygen atoms and the atomic model of missing oxygen to simulate the oxygen vacancy, where a relaxation model was applied to set the relative positions of oxygens with the lowest energy states. Legends of atomic models in Figure. 21c

represents 3 full oxygen atoms bonded to the metal ion (dotted lines) and the vacancy-incorporated atomic structure (solid lines) as the “fully bonded” and the “oxygen-vacancy relaxed”, respectively.

Graphs of DS3 and DS4 values are very similar and look like a single line, except for the difference visible in the small Fermi level range. As expected, the fully bonded DS1, where the growth of Ga_2O_3 follows the stacking sequence of Al_2O_3 , is more stable than any other 3 interface stackings, with the formation energy values of 4.1 eV/f.u.(formula unit) for DS3 and DS4, and 9.64 eV/f.u. for DS2. According to classical nucleation theory, the probability of metastable nucleation (I_{meta}) is determined by the Arrhenius equation $I_{meta} \sim \exp(-\Delta E/kT)$, which indicates that DS2 configuration can be formed in the substrate in rare probability. This is supported by experimental results shown in Figure. 21d-g. Based on this examination, most domains should follow the stacking sequence of Al_2O_3 with DS1 configuration because ΔE for the stacking sequence of DS3, DS4, and DS2 is much higher than kT . When the oxygen vacancies are considered, which is shown in solid lines in Figure. 21c, DS1 configuration is still more stable, 0.4 and 9.19 meV/f.u., lower than any other.

Formation of the anti-phase domain may be related to the relative formation energy between domain stacking configurations. Consider triangular nucleation on Al_2O_3 (001) with aluminum atom positions coincides with the triangle corners (Figure. 18). When one of the corners has a situation of higher

bonding energy of Al-O, such as DS3 and DS4 configurations as investigated above, vacancy formation, and surface steps, the corner with higher formation energy may transit to preferential bonding to the other side of the triangle, which ends up as an inverted triangle. (For example, as shown in Figure. 18, when 2 corners of the yellow triangle have the same formation energy except for the corner “P”, triangular bonding will be maintained along one direction. However, if the “P” corner has higher formation energy or different surface termination atoms from a surface step, bonding to the “P” corner of the triangle may be less probable than for the “Q” corner, and then, it may be a seed for the inverted domains.) Any instability of one corner of the metal ion triangle may create inverted nuclei.

However, the energy difference between IPD and APD is minimized in the non-stoichiometric case. That is, if oxygen vacancies are involved in the nucleation process, the nucleation probability of APD can be enhanced.

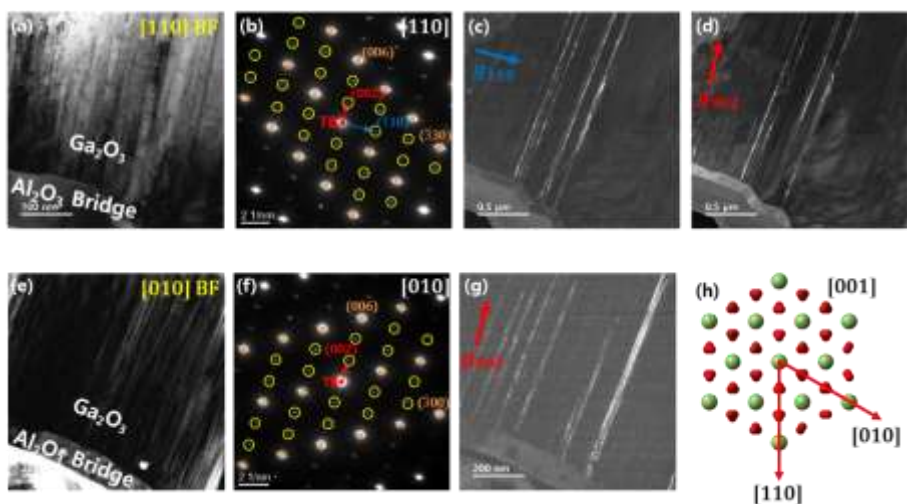


Figure. 14 TEM images and electron diffraction from two observation directions from single-crystal alpha Ga_2O_3 . (a)-(d) are obtained in $[110]$ zone axis. (a) Bright-field image. (b) Electron diffraction image of (a). (c) Dark field image of g_{110} . (d) Dark field image of g_{002} . (e)-(g) are obtained in $[010]$ zone axis. (e) Bright-field image. (f) Electron diffraction image of (e). (g) Dark field image of g_{002} . (h) $[001]$ zone atomic model of alpha- Ga_2O_3 .

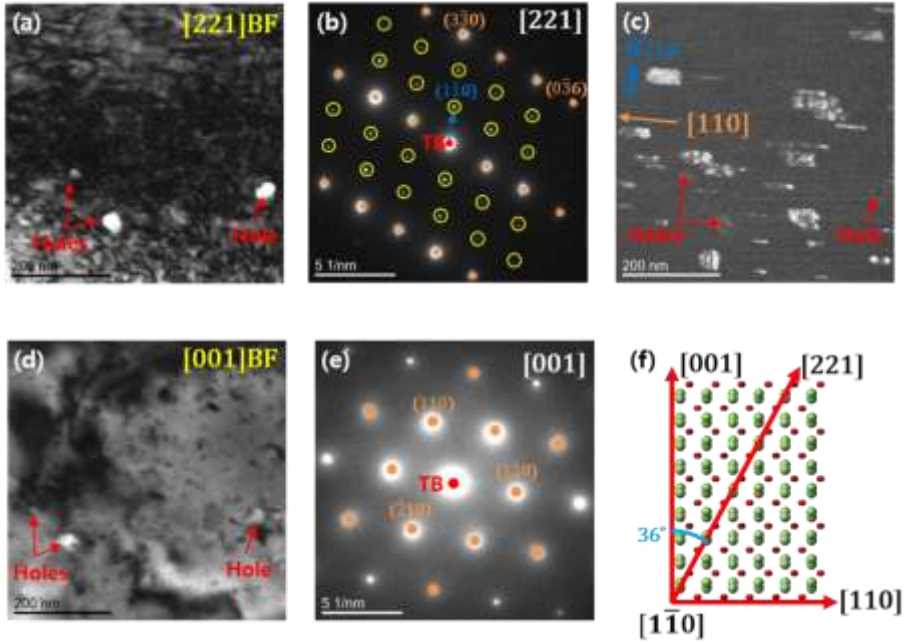


Figure. 15 **TEM images and electron diffraction from two observation directions from single-crystal alpha Ga_2O_3 .** (a)-(c) are obtained in [221] zone axis. (a) Bright-field image. (b) Electron diffraction image of (a). (c) Dark field image of g_{110} . (d), (e) are obtained in [001] zone axis. (d) Bright-field image. (e) Electron diffraction image of (d). (f) Schematic diagram of three zones observed, [110], [221] and [001].

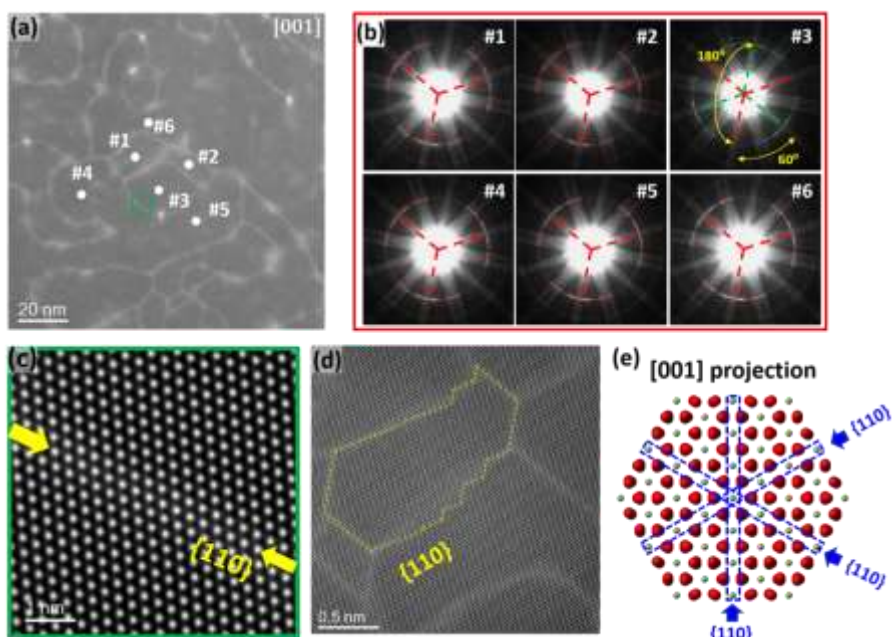


Figure. 16 **Confirmation of relative orientation relations using converted beam electron diffraction(CBED).** (a) ADF image was taken near the area where the extra diffraction spots were observed. (b) The CBED image indicated by numbers are shown in (b). (c) Atomic-resolution ADF image indicated by a green box in (a). (d) Atomic-resolution ADF image in lower magnification. (e) [001] zone atomic model of α -Ga₂O₃.

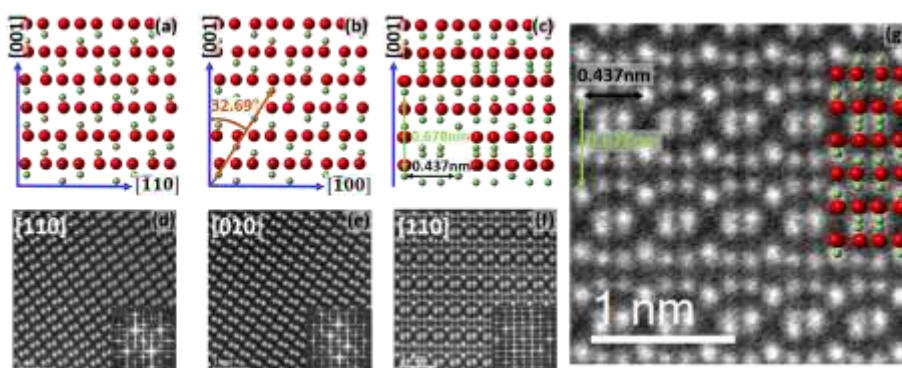


Figure. 17 **Origin of extra diffraction spots.** (a), (b) show atomic models of $\alpha\text{-Ga}_2\text{O}_3$ viewed along [110] and [010], respectively. (c) is an atomic model of [110] and [010] crystal overlapped. (d), (e) are ADF images observed from [110] and [010] zone, respectively, with FFT in the insets. (f) is the ADF images of the extra diffraction area (the inset is the FFT results). (g) is an enlarged ADF image of (f) with an atomic model overlayed.

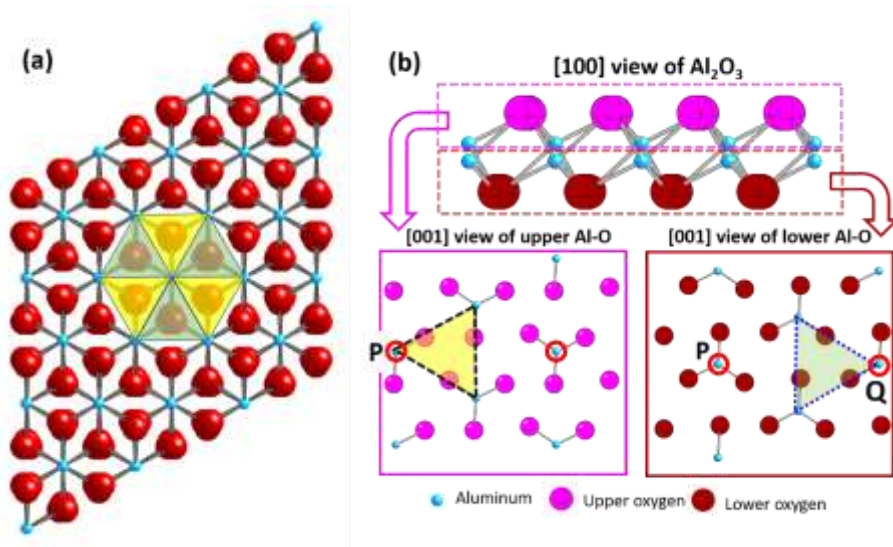


Figure. 18 **Formation mechanism of the anti-phase domains.** (a) An atomic model of Al_2O_3 viewed from $[001]$. Perfect Al_2O_3 crystals have 3-fold bonding of Al-O with equilateral oxygen triangles with aluminum in the recessed position at the center of the oxygen triangle. The crystallographic orientation of the triangles may have 120-degree or 180-degree symmetry as indicated using semitransparent yellow and green, respectively. (b) The surface of the (001) Al_2O_3 has either an aluminum-terminated surface or the oxygen-terminated one. Pink oxygen represents the oxygen-terminated configuration and aluminum-terminated in brown, where aluminum is sky blue. When the aluminum-terminated layer of Al-O triangular bonding is removed, the next Al-O bonding reveals oxygen-terminated and inverted triangle geometry. Two possible configurations of inverted triangles, marked with dotted lines, are shown. The probability of forming the in-phase and anti-phase domains may be the same because both terminations have the same lateral distance between Al-O.

Depending on the bonding direction (either “P” or “Q”) anti-phase domain may be formed. The bonding direction can be affected by factors, such as the formation energy of Al-O, surface steps, and oxygen vacancies, which determine the orientation of the nuclei.

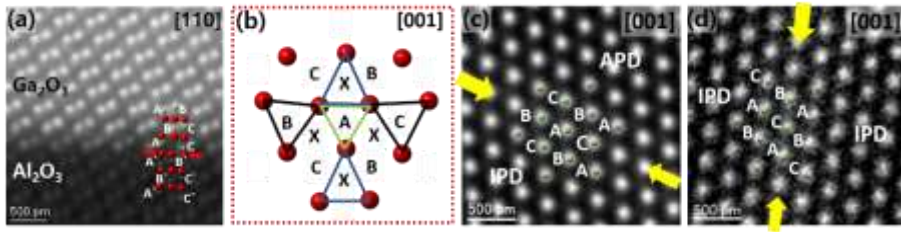


Figure. 19 **Observation of atom configuration of anti-phase domain boundary and in-phase domain boundary.** (a) ADF image of the in-phase domain $\text{Al}_2\text{O}_3/\text{Ga}_2\text{O}_3$ interface and the corresponding atomic model at $[110]$ zone. (b) An atomic model, viewed along $[001]$, of the interface marked by the red arrow in (a). A, B, and C are hollow sites centered on equilateral oxygen triangles, which are the same stacking sites as Al_2O_3 . X are hollow sites centered on isosceles oxygen triangles different from the stacking site as Al_2O_3 . (c) and (d) Atomic-resolution ADF Images and the corresponding atomic positions viewed at $[001]$ zone of anti-phase domain and in-phase domain boundary, respectively. The yellow arrows in (c) and (d) indicate the location of the high-contrast $\{110\}$ boundaries. When comparing the relative number density of gallium atoms from the arrow-marked plane and others, it does not give any fluctuations in the number of gallium atoms, regardless of the boundary type, anti-phase domain or in-phase domain boundaries.

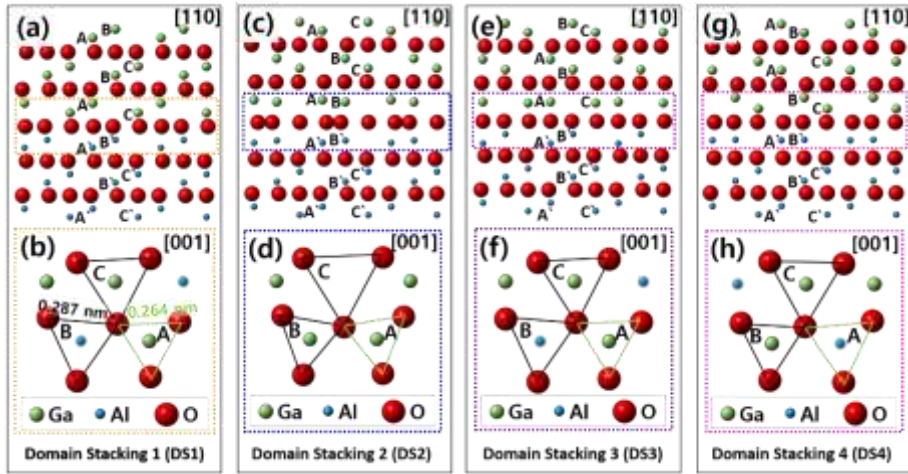


Figure. 20 Atom configurations of possible configurations of Al-O stacking.

Atomic models of Ga_2O_3 on Al_2O_3 viewed from $[110]$ ((a), (c), (e), and (g)) and viewed from $[001]$ ((b), (d), (f), and (h)). (a), (b) Atomic models of Ga_2O_3 stacking sequence same as Al_2O_3 (named as DS1 with $A'B'(Al_2O_3)/(Ga_2O_3)CA-BC-AB$ stacking). (c),(d) DS2 atomic stacking of $A'B'(Al_2O_3)/(Ga_2O_3)BA-CB-AC$, (e),(f) DS3 atomic stacking of $A'B'(Al_2O_3)/(Ga_2O_3)AC-BA-CB$, and (g),(h) DS4 stacking of $A'B'(Al_2O_3)/(Ga_2O_3)CB-AC-BA$.

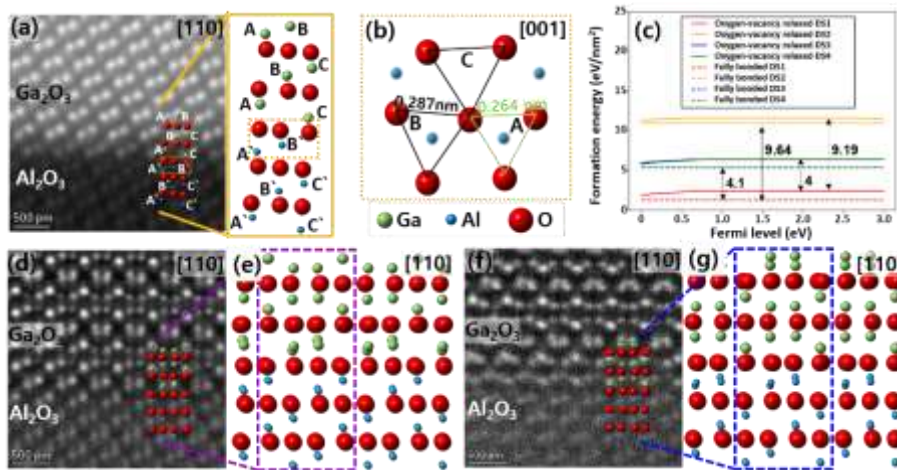


Figure. 21 **Origin of anti-phase domain.** (a) High-resolution ADF image of the typical Al₂O₃/Ga₂O₃ interface with the corresponding atomic model overlaid on [110] zone. (b) atomic model of the interface viewed along [001] in the regions marked with dotted-rectangular with orange in (a). (c) Calculated boundary formation energies based on the atomic model shown in Figure. 20. (d), (e) ADF image of domain stacking3(DS3) of Al₂O₃/Ga₂O₃ interface and the corresponding atomic model at [110] zone, and an atomic model with DS1 and DS3 overlapped, respectively. (f), (g) ADF image of the DS4 of Al₂O₃/Ga₂O₃ interface and the corresponding atomic model at [110] zone with DS1 and DS4 overlapped.

3. 5. Summary

In summary, a high-quality alpha-Ga₂O₃ thin film was grown on the membrane of the Al₂O₃ single-crystal substrate. Hetero-epitaxial alpha Ga₂O₃ crystals are nucleated and grown with 3-fold symmetry based on the template provided by Al₂O₃. APDs were found, and these may be formed at an early stage of growth based on the oxygen templates provided from the Al₂O₃ surface; they were found to have 180-degree inverted configurations from the surroundings. These APDs lead to extra diffraction spots when observed along [110] and [010], and can identify using higher-order Laue zone reflections in CBED.

3. 6. Bibliography

- ¹ D. H. Yan, G. F. Yin, Z. B. Huang, X. M. Liao, Y. Q. Kang, Y. D. Yao, B. Q. Hao, J. W. Gu, and D. Han, *Inorg Chem* **48** (14), 6471 (2009).
- ² K. Shimamura, E. G. Villora, K. Domen, K. Yui, K. Aoki, and N. Ichinose, *Jpn J Appl Phys* **2** **44** (1-7), L7 (2005).
- ³ T. Oshima, T. Okuno, and S. Fujita, *Jpn J Appl Phys* **1** **46** (11), 7217 (2007).
- ⁴ M. Orita, H. Ohta, M. Hirano, and H. Hosono, *Appl Phys Lett* **77** (25), 4166 (2000).
- ⁵ M. Higashiwaki, K. Sasaki, A. Kuramata, T. Masui, and S. Yamakoshi, *Appl Phys Lett* **100** (1) (2012).
- ⁶ S. I. Stepanov, V. I. Nikolaev, V. E. Bougrov, and A. E. Romanov, *Rev Adv Mater Sci* **44** (1), 63 (2016).
- ⁷ R. Roy, V. G. Hill, and E. F. Osborn, *J Am Chem Soc* **74** (3), 719 (1952).
- ⁸ J. G. Zhang, B. Li, C. T. Xia, G. Q. Pei, Q. Deng, Z. H. Yang, W. S. Xu, H. S. Shi, F. Wu, Y. Q. Wu, and J. Xu, *J Phys Chem Solids* **67** (12), 2448 (2006).
- ⁹ E. G. Villora, K. Shimamura, Y. Yoshikawa, K. Aoki, and N. Ichinose, *J Cryst Growth* **270** (3-4), 420 (2004).
- ¹⁰ V. I. Vasylytsiv, Y. I. Rym, and Y. M. Zakharko, *Phys Status Solidi B* **195** (2), 653 (1996).
- ¹¹ N. Ueda, H. Hosono, R. Waseda, and H. Kawazoe, *Appl*

- Phys Lett **70** (26), 3561 (1997).
- ¹² Y. Tamm, P. Reiche, D. Klimm, and T. Fukuda, J Cryst Growth **220** (4), 510 (2000).
- ¹³ N. Suzuki, S. Ohira, M. Tanaka, T. Sugawara, K. Nakajima, and T. Shishido, Physica Status Solidi C – Current Topics in Solid State Physics, Vol 4 No 7 2007 **4** (7), 2310 (2007).
- ¹⁴ K. Irmscher, Z. Galazka, M. Pietsch, R. Uecker, and R. Fornari, J Appl Phys **110** (6) (2011).
- ¹⁵ D. Yang, B. Kim, T. H. Lee, J. Oh, S. Lee, W. Sohn, E. Yoon, Y. Park, and H. W. Jang, Acs Appl Electron Ma **3** (10), 4328 (2021).
- ¹⁶ D. Yang, B. Kim, T. H. Eom, Y. Park, and H. W. Jang, Electron Mater Lett **18** (2), 113 (2022).
- ¹⁷ D. Shinohara and S. Fujita, Jpn J Appl Phys **47** (9), 7311 (2008).
- ¹⁸ S. D. Lee, K. Akaiwa, and S. Fujita, Phys Status Solidi C **10** (11), 1592 (2013).
- ¹⁹ J. Kim, D. Moon, S. Lee, D. Lee, D. Yang, J. Jang, Y. Park, and E. Yoon, Appl Phys Lett **112** (21) (2018).
- ²⁰ J. Jang, D. Yang, D. Moon, D. Choi, H. J. Lim, S. G. Kang, D. Bae, H. N. Han, Y. Park, and E. Yoon, J Cryst Growth **498**, 130 (2018).
- ²¹ J. Jang, D. Moon, H. J. Lee, D. Lee, D. Choi, D. Bae, H. Yuh, Y. Moon, Y. Park, and E. Yoon, J Cryst Growth **430**, 41 (2015).
- ²² C. G. Van de Walle and J. Neugebauer, J Appl Phys **95** (8),

- 3851 (2004).
- ²³ K. Morizane, *J Cryst Growth* **38** (2), 249 (1977).
- ²⁴ H. Wondratschek and W. Jeitschko, *Acta Crystallogr A* **32** (Jul1), 664 (1976).
- ²⁵ Y. W. Kim, D. H. Mei, D. Lubben, I. Robertson, and J. E. Greene, *J Appl Phys* **76** (3), 1644 (1994).
- ²⁶ S. J. Pennycook, *Annu Rev Mater Sci* **22**, 171 (1992).
- ²⁷ N. D. Browning, M. F. Chisholm, and S. J. Pennycook, *Nature* **366** (6451), 143 (1993).
- ²⁸ J. M. Zuo, A. B. Shah, H. Kim, Y. F. Meng, W. P. Gao, and J. L. Rouviere, *Ultramicroscopy* **136**, 50 (2014).
- ²⁹ P. J. Phillips, M. De Graef, L. Kovarik, A. Agrawal, W. Windl, and M. J. Mills, *Ultramicroscopy* **116**, 47 (2012).
- ³⁰ D. D. Perovic, C. J. Rossouw, and A. Howie, *Ultramicroscopy* **52** (3-4), 353 (1993).

Chapter 4. Luminescence properties related anti-phase domain of high crystalline alpha-Ga₂O₃

4. 1. Introduction

Gallium oxide is an ultra-wide band gap semiconductor with a high breakdown electric field. It has attracted attention for its capability for high current-high speed switching with low loss, UV transparent electrodes, and solar-blind ultraviolet photodetectors.¹⁻⁵ Gallium oxide is known to exhibit six crystal structures, including monoclinic(β), corundum(α), spinel(γ), two orthorhombic(ϵ , δ), and a transient polymorph κ phases, which is an analog of orthorhombic-Al₂O₃.^{6, 7}

Early research dominated β -Ga₂O₃ because it was possible to grow high crystalline thin films in thermodynamic stability, but the substrate required expensive processes and was challenging to use large-area fabrication.⁸⁻¹⁴ In a recent study, although α -Ga₂O₃ is known as a thermodynamically metastable phase, α -Ga₂O₃ has been spotlighted as practical material because high-quality thin film can be grown using the widely used sapphire substrate.^{3, 15-18} Therefore, growing α -Ga₂O₃ thin film on an inexpensive sapphire substrate is the best choice for practical Ga₂O₃ device fabrication.^{15, 16, 18}

Generally, device defects deteriorate performance, such as current

leakage or breakdown paths, leading to lower efficiency and poor reliability.^{19,}

²⁰ Therefore, the correlation between physical properties and the defects in α -Ga₂O₃ films is needed to identify, which is the first step to designing and fabricating reliable and high-performance devices.

In this chapter, we report the luminescence characteristics of domain boundaries of α -Ga₂O₃ using cathodoluminescence (CL) in transmission electron microscopy (TEM) and density functional theory (DFT) calculation.

4. 2. Experimental and analysis detail

Al_2O_3 nanomembranes were prepared in tent-shaped channels along [110] on a 2-inch sapphire wafer. Rectangular thin-film line patterns of photoresist (PR) with a height and width of $2\mu\text{m}$ in cross-section were fabricated using photolithography on a c-plane sapphire substrate. An amorphous alumina layer of 60nm deposited on PR-patterned sapphire substrates using atomic layer deposition (ALD) at 110°C with trimethylaluminum (TMA) and deionized (DI) water as sources of Al and O, respectively. The ALD-deposited substrate was dipped in acetone and rinsed with DI water to remove PR. The perimeter of the substrate was scribed with a diamond pencil to open a channel inside chemicals and air. Finally, the sample was annealed in a tube furnace at 1150°C for 12 hours to crystallize amorphous alumina to $\alpha\text{-Al}_2\text{O}_3$ by solid phase epitaxy (SPE).²¹⁻²³

$\alpha\text{-Ga}_2\text{O}_3$ thin films were grown on a stripe-shaped sapphire nanomembrane substrate using mist CVD. The CVD was equipped with homemade, horizontal thermal-wall-type precursor vaporizers, which consisted of two ultrasonic transducers to atomize the water-based source for the growth of Ga_2O_3 . The Ga precursor is gallium acetylacetonate ($\text{Ga}(\text{acac})_3$, $\text{Ga}(\text{C}_5\text{H}_7\text{O}_2)_3$), mixed with DI water and atomized, and transferred to the reactor. The Oxygen source was provided from O_2 gas, diluted to a

concentration of 0.05 mole/L, and mixed with 1 vol% of hydrochloric acid (HCl). N₂ is a carrier diluent gas with three standard liters per minute (SLM) flow rates and 0.5 slm, respectively. The growth performs at 450 °C.^{15, 16}

The XRD results of as-grown alpha Ga₂O₃ confirm the existence of single-crystal alpha-Ga₂O₃ is highly crystallinity (Figure. 9).

TEM specimens were prepared by mechanical grinding/polishing, after which they were ion-polished using a 3keV beam and a commercially available ion-polishing system (Gatan 691). The samples as well as the viewing planes are schematically presented in Figure. 22, along with the corresponding annular dark field (ADF) zone images.

Conventional TEM Images, electron diffraction (ED), and convergent beam electron diffraction (CBED) were taken using a JEM-2100F TEM (Japan Electron Optics Limited) operated at 200kV. Atomic-resolution ADF and images were obtained using a Themis-Z Cs-corrected TEM (Thermo-Fischer) operated at 200kV. Cathodoluminescence (CL) spectrum imaging was obtained using a home-built CCL system combined with a JEM-2100F scanning transmission electron microscopy (STEM) operated at 120kV. A CL spectrum of 128x128 pixels was acquired at room temperature with a 6ms dwell time on each pixel.

The CL system comprises a mirror and an optical fiber connected to an external optical fiber. The mirror—, which encapsulates the sample and guides the generated signal to the optical fiber—can be moved over the sample

to locate the CL collection area. The total thickness of the CL system is 2.5 mm at the sample position to avoid any interference within the objective pole. The collected signal was processed using a Shamrock 163 spectrometer and a Newton 971 electron-multiplier charge-coupled device (Andor, Oxford).

The density functional theory (DFT) calculations performed the Vienna ab initio simulation package (VASP). A projector-augmented wave (PAW) method is used for interactions between the valence electrons and the ionic cores. The generalized gradient approximation (GGA) in the Perdew-Burke-Ernzerhof (PBE) formulation was used for exchange-correlation function. The electron wave function expands a base set of plane waves with a kinetic energy cut off 500 eV. The redefined $\text{Ga}_2\text{O}_3/\text{Al}_2\text{O}_3$ boundary models with 60 atoms, with an $8 \times 8 \times 2$ gamma-centered k-point set, were fully relaxed until all energies were smaller than 0.01 eV/Å (by fully relaxing the atomic positions and lattice parameter).

With a $4 \times 6 \times 2$ gamma-centered k-point set, the redefined anti-phase domain boundary models were fully relaxed with 240 atoms until they were smaller than 0.01 eV/Å (by fully relaxing only the atomic positions with fixed experimental lattice parameters). The convergence threshold for the self-consistent field (SCF) iteration was set at 10^{-7} eV. Spin-constrained calculations were conducted for all models.

The formation energy was calculated based on the following formula.²⁴

$$E^f(q, E_F) = E_{tot}(q) - \sum_i n_i \mu_i + qE_v + qE_F$$

where E^f is the formation energy, E_{tot} is the total energy of the defect cell, n_i is the number of i atoms in the supercell, μ_i is the corresponding chemical potential, q is the charge state of the defect, E_v is the energy of the valence-band maximum in bulk, and E_F is the Fermi level defined to be zero at the bulk valence-band maximum.

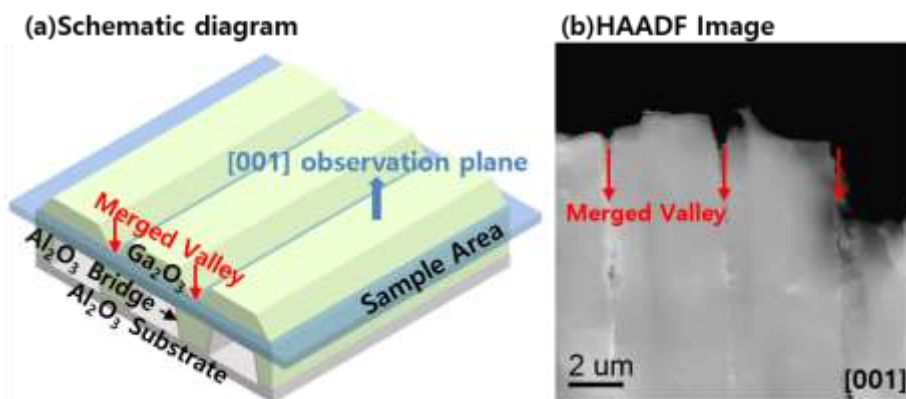


Figure. 22 (a) Schematic diagram of prepared TEM samples. (b) ADF image of prepared TEM samples in [001].

4. 3. Results and discussions

Figure. 23a shows a schematic view of the sampling area with a brightfield image obtained from [001] zone plan-view TEM in Figure. 23b, where the merged valleys are visible, and the electron diffraction pattern exhibits a high crystalline single-crystal pattern in the inset. When the dotted yellow circle area in Figure. 23b is magnified, and white contrast was visible as can be seen in Figure. 23c (intermediate magnification between Figure. 23b and c can be seen in Figure. 24). The nature of the boundaries is investigated using convergent beam electron diffractions (CBED) to identify the relative crystallographic orientational relationship between boundaries, and the results are shown in Figure. 23d. CBED patterns, from six different positions marked with corresponding numbers in Figure. 23c, reveal anti-phase domains (APD) determined from Higher-Order Laue Zones (HOLZ) patterns. All domains exhibit 3-fold symmetry, but #1 exhibits a 180-degree inversion (as if rotated by 60 degrees because of the hexagonal symmetry) relative to the surrounding domains.²⁵ Figure. 16c shows an atomic-resolution ADF image of the area of the green box in Figure. 16a, obtained from C_s-Corrected TEM, where high contrast can be seen in domain boundaries in ADF. If the boundary contrast of domains is due to the elemental fluctuation, it is expected to see higher contrast in atomic resolution ADF image, but no distinct ADF contrast was observed as seen in Figure. 16c. The lower magnification image reveals domain boundaries

with facets on $\{110\}$ planes, as shown in Figure. 16d, whose planes are schematically represented in Figure. 16e. The boundaries do not show equiaxed shapes, and instead, they appear elongated, because they are close to the region around the Merged Valley marked in Figure. 23a (See also Figure. 24), in which the two growth directions of $[001]$ and $[110]$ meet.^{26,27} The contrast is believed to come from the merging boundaries of rotated domains; this will be detailed in a later section.

The luminescence characteristics in the anti-phase domains are investigated using CL in TEM. Luminescence characteristics from a large area, with two different exposure times of 2 and 10 seconds, are shown in Figure. 25a and b, respectively, obtained from the region of the area circled in red in Figure. 23b. Asymmetric shoulders are observed at 350nm, 380nm, 410nm, 440nm, 470nm, and a long tail of wavelength.

In a high-energy UV region below 300nm, the spectra intensity attenuates rapidly due to absorption from the series of optical components - the lens mounted to collimated lights in the main CL system, optical fiber, and light collection stages of the CCD camera. When the spectra collection time was extended to 10 s, it was possible to obtain and confirm the existence of the UV peak of $\sim 223\text{nm}$ (5.56eV), as indicated by the arrow in Figure. 25b. As the band-edge energy of alpha Ga_2O_3 is reported as 4.9-5.6eV (263nm-217nm), the 223nm peak is considered a near band-edge transition.²⁸⁻³¹ Figure. 25c is the

same image as Figure. 23b, where a red dot marks the location of the APD.

Figure. 25d is the characteristic wavelength mapping of the inside domain, and Figure. 25e-i show spectrum images (SI) that have been extracted with specific wavelengths based on the asymmetric wavelength shoulder observed in Figure. 25a. Figure. 25j shows the overlapped images of 320nm, 350nm, and 380-480nm wavelengths over the ADF image using red, blue, and green, respectively. A strong 320nm peak is observed within the domain, while 380-480nm peaks are more strongly detected at the domain boundary. The APD boundary exhibits a singular luminescence of a characteristic wavelength of 350nm, which appeared purple in Figure. 25j.

Bright contrast at the domain boundary may lead to higher concentrations of gallium at the boundaries, but EELS mapping shows no difference in gallium concentration (Figure. 26a-c).^{32, 33} In addition, the atom configuration of the APD boundary and domain boundary shown in Fig. 19, shows no change in the gallium contents at the boundary when looking at [001]. As shown in Figure 26e-h, we observed a change in the contrast of domain boundaries while changing the ranges of the ADF's collection angles, from 40-200 mrad to 81-200 mrad. The results confirm that the bright contrast of domain boundaries originated from local strains.³⁴⁻³⁶ Mosaic structure is commonly observed in the lattice-mismatched heteroepitaxy, which is also observed in this Ga₂O₃/Al₂O₃ system as well. The level of the mosaic rotation, however, is much

less than the thick substrate of Al_2O_3 because the strain is partially observed by the thin membrane substrate of Al_2O_3 . In a thick substrate, most of the mismatch is accommodated by the thin film, while the strain is shared in the film and the substrate by the fraction of the relative thickness.

The lattice mismatch between Al_2O_3 (JCPDS card no. 10-173) and Ga_2O_3 (JCPDS card no. 043-1013) on $(\bar{3}30)$ is known as 4.61% and the number density of threading dislocations is far less than expected as observed in a high-resolution cross-sectional image (Figure. 27). It is believed that the lattice mismatch is relieved from multiple sources, in combinations of threading dislocation formation, strain accommodation from thin membrane substrate, and mosaic structure of domains, which is typically observed in hetero-epitaxial growth. The evidence of the rotation can be seen in the enlarged diffraction spot shown in the inset of Figure. 25d, where the crystallographic rotation of ~ 2.5 degrees is visible along $[001]$. The rotation of each domain means that the crystallographic orientation is set at the nucleation stage, with triangular templates provided by the membrane Al_2O_3 . As the nucleated islands of Ga_2O_3 grow and cover the Al_2O_3 substrate, domain boundaries are formed when they merge. Boundaries inevitably create in-plane lattice mismatch because the atomic positions do not coincide with the crystallographic rotation. (Figure. 28)

Figure. 29a and b show the corresponding spectra with Gaussian decomposition, based on the three regions with distinct luminescence characteristics – inside the domain, domain boundary, and APD boundary as

shown in Figure. 25j. Although the height and position of peaks vary slightly from area to area, 320nm, 380nm, 410nm, 440nm, 470nm, and a long wavelength tail are commonly observed in the three areas. Except for the 350nm peak, all other peaks are similar to those previously reported.^{1,19,37-39} The State-transition from these six commonly observed peaks may come from native point defects such as oxygen and gallium vacancy.³⁷⁻³⁹ The origin of the 350nm peak from CL data was previously reported on Hydride vapor phase epitaxy (HVPE) grown Sn-doped α -Ga₂O₃.³⁸ In our study, no intermediate states were expected from doping because no doping was implemented, the 350nm peak in this study originates from a different defect state. The Total density of states calculated using ab-initio methods is shown in Figure. 29c-f, where a defect state of 0.52eV forms near the valance band at the APD boundary. Although the intermediate defect state of 0.52eV does not exactly match to produce the single transition giving 350nm, which is equivalent to 3.54eV, Gaussian decomposition results (Figure. 29b) support the 350nm peak and the defect state.

Therefore, the 350nm peak is believed to come from trap-to-trap transition related to the states formed by local strain, which is originated by the instability of Al-O bonding to rotate nuclei 180 degrees.

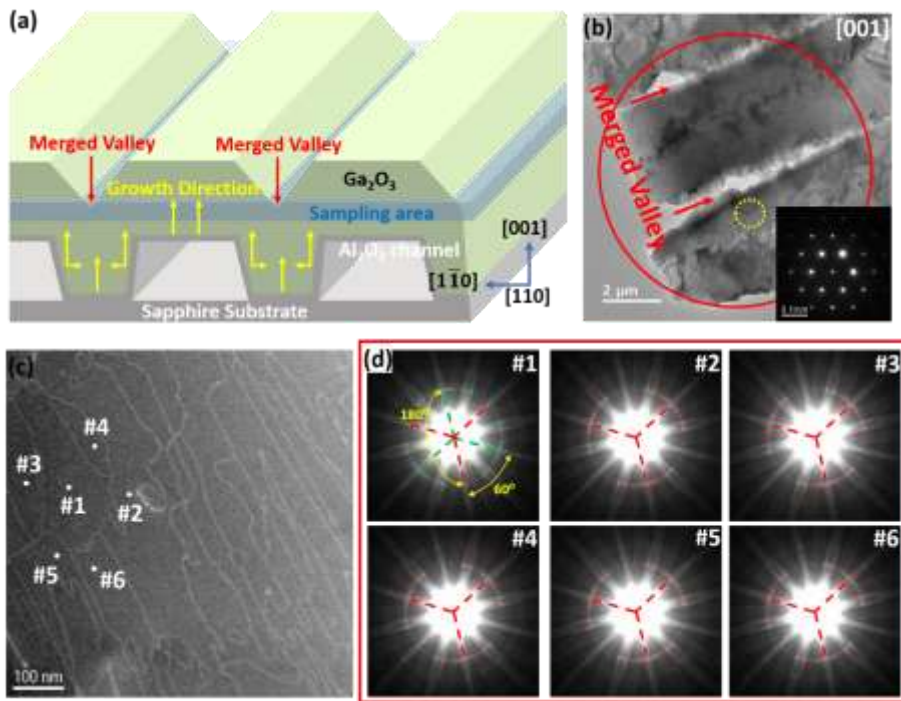


Figure. 23 **Microstructure observed from [001] zone plan-view TEM.** (a) Schematic diagram of plan-view TEM (PTEM) sampling area. (b) Low magnification brightfield TEM image of the area analyzed. Electron diffraction from the dotted circle is shown in the inset. (c) Annular darkfield (ADF) image showing boundaries, with (d) CBED patterns with corresponding numbered regions marked in (c).

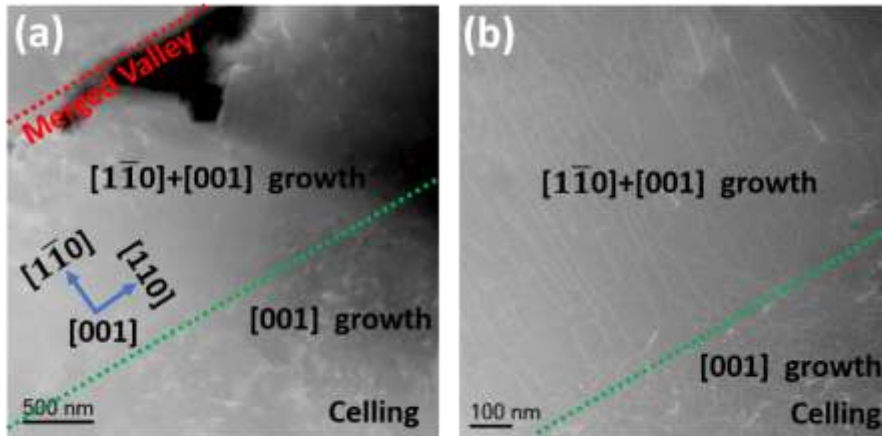


Figure. 24 (a) Low magnification HAADF image near the merged valley. (b) is an enlarged HAADF image to show the geometry of domain boundaries. Domains are developed along the growth direction as indicated in Figure. 23a and depending on the sampling region, two distinct regions, equiaxed and elongated boundaries, are visible.

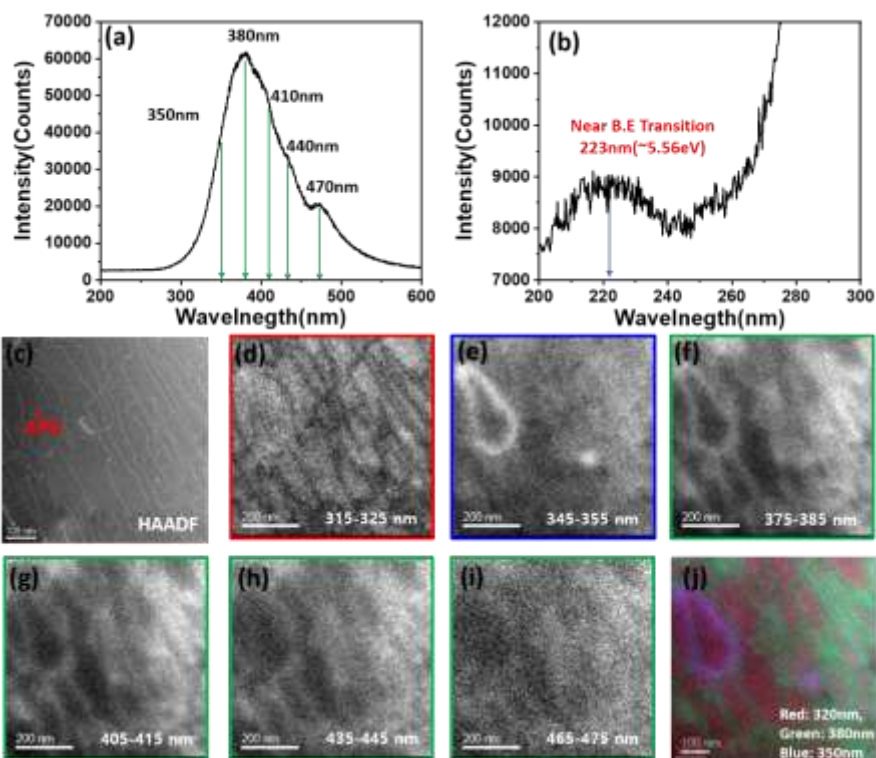


Figure. 25 **Luminescence characteristics in Plan-view TEM.** (a),(b) Luminescence spectra obtained from the red circle area in Fig. 1(b) exposed electron beam for 2s and 10s, respectively. (c) ADF image used for CL analysis. (d)-(j) show a 2-dimensional mapping of a specific wavelength range, which is shown at the bottom of the figures.

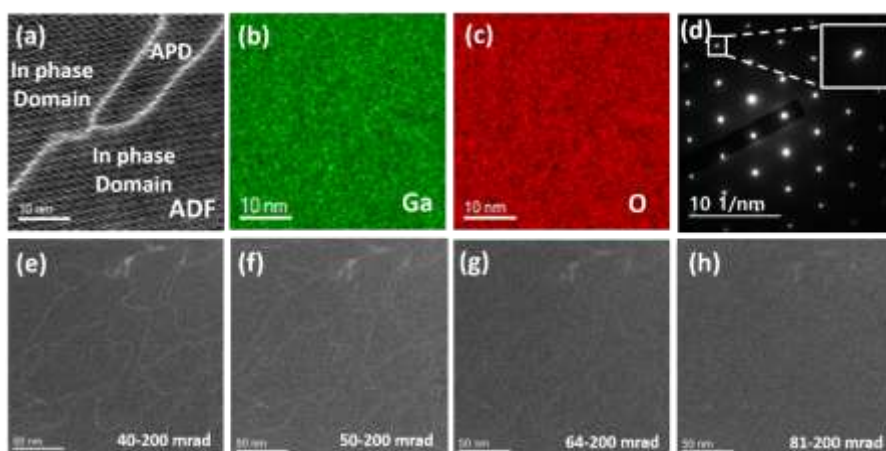


Figure. 26 **Origin of boundary contrast.** (a) ADF image showing bright boundary contrast. (b), (c) are the gallium and oxygen electron energy loss spectroscopy (EELS) elemental mappings of the area shown in (a), respectively. (d) electron diffraction pattern at [001] zone, where the rotation of the domains is confirmed from the mosaic pattern of the diffraction spots as shown in the inset. (e)-(h) are ADF images with different ranges of collection angles. Collection angles are listed at the bottom of the figure.

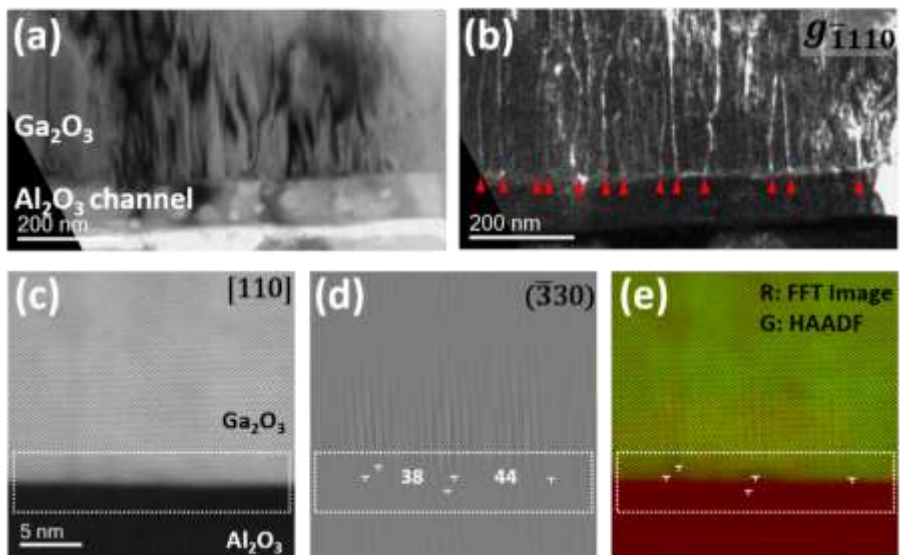


Figure. 27 (a),(b) Low magnification two beam brightfield and dark field image of cross-section TEM with diffraction vectors of $g_{\bar{1}110}$, where threading dislocations, marked with arrows, are visible. (c) High-resolution image of the interface to visualize the existence of the threading dislocations, and (d) the reconstructed image using $(\bar{3}30)$ after the filtering Fast Fourier-Transformed (FFT) image. (e) colorized image of FFT-reconstructed and ADF using red and green. Theoretical calculation gives one threading dislocation per 21.6 planes of $(\bar{3}30)$, but actual measurement reveals threading dislocations in every ~ 38 and ~ 44 $(\bar{3}30)$ planes, which means that the relief from the lattice mismatch was additionally relieved by the thin membrane substrate and mosaic domain structure formation.

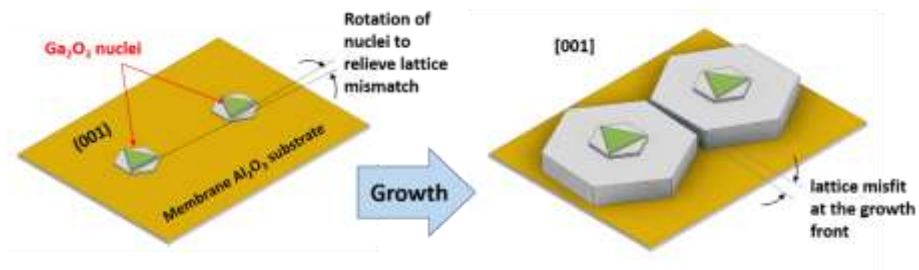


Figure. 28 **Formation of in-plane rotation and the development of strain at the merging boundary.** (a) In the nucleation stage, a mosaic structure is developed to accommodate the lattice mismatch partially between the substrate and the film. (b) As the crystal grows in vertical and lateral directions, the crystal maintains the rotation and the lattice mismatch builds strain at the merging front.

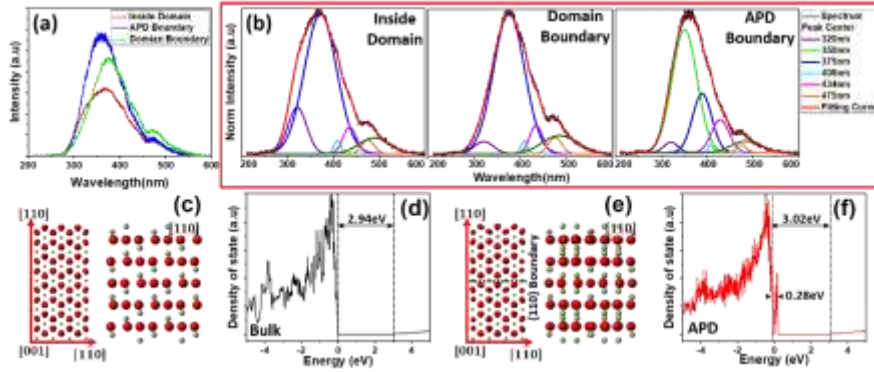


Figure. 29 **Variations of Luminescence characteristics.** (a) Areal spectrum from inside domain, domain boundary, and APD boundary. (b) Gaussian deconvolution of each area spectrum of (a). It is fitted by seven Gaussian peaks corresponding to asymmetric shoulder and the relative peak heights reveal the difference in the energy states in 3 major areas of (a). (c) and (d) show the atomic model of [001] and [110] view, and the calculation results of the total density of states in the pristine bulk, respectively. (e) and (f) are for the anti-phase domain boundary of α -Ga₂O₃.

4. 4. Summary

A high-quality alpha-Ga₂O₃ thin film was grown on an Al₂O₃ single-crystal thin-wall channel structure. Hetero-epitaxial alpha Ga₂O₃ crystals are nucleating and grown with 3-fold symmetry based on the template provided by Al₂O₃, and the domain boundaries are formed from the small rotation of the mosaic structure. The APD confirmed by CBED is believed to be developed at the stage of nucleation based on the unstable, or uneven Al-O templates provided by the Al₂O₃ surface. The domain and APD boundaries exhibit bright contrast in ADF, which originates from a local strain of crystallographic rotation and not from the local elemental fluctuations of gallium. As confirmed by CL measurement in TEM, the bandgap energy of alpha-Ga₂O₃ is inferred to be 5.56 eV with a near band edge transition of $\sim 223\text{nm}$. Although the heights and positions of peaks vary slightly from area to area, the luminescence peaks at 320nm, 380nm, 410nm, 440nm, 470nm, and a long tail of wavelength are commonly observed throughout the crystal - inside the domain, domain boundaries, and APD boundary, where the distinct 350nm peak was observed at the APD boundary. Misorientation between domains was found, which leads to an in-plane mismatch in crystallographic lattices at the boundary when the two misoriented domains grow and the growth front merges. The imperfect lattice structure at the boundary is believed to create intermediate states.

4. 5. Bibliography

1. Yan, D.H., et al., *Biom mineralization of Uniform Gallium Oxide Rods with Cellular Compatibility*. Inorganic Chemistry, 2009. **48**(14): p. 6471–6479.
2. Shimamura, K., et al., *Epitaxial growth of GaN on (100) beta-Ga₂O₃ substrates by metalorganic vapor phase epitaxy*. Japanese Journal of Applied Physics Part 2–Letters & Express Letters, 2005. **44**(1–7): p. L7–L8.
3. Oshima, T., T. Okuno, and S. Fujita, *Ga₂O₃ thin film growth on c-plane sapphire substrates by molecular beam epitaxy for deep-ultraviolet photodetectors*. Japanese Journal of Applied Physics Part 1–Regular Papers Brief Communications & Review Papers, 2007. **46**(11): p. 7217–7220.
4. Orita, M., et al., *Deep-ultraviolet transparent conductive beta-Ga₂O₃ thin films*. Applied Physics Letters, 2000. **77**(25): p. 4166–4168.
5. Higashiwaki, M., et al., *Gallium oxide (Ga₂O₃) metal–semiconductor field-effect transistors on single-crystal beta-Ga₂O₃ (010) substrates*. Applied Physics Letters, 2012. **100**(1).
6. Stepanov, S.I., et al., *Gallium Oxide: Properties and Applications – a Review*. Reviews on Advanced Materials Science, 2016. **44**(1): p. 63–86.

7. Roy, R., V.G. Hill, and E.F. Osborn, *Polymorphism of Ga₂O₃ and the System Ga₂O₃-H₂O*. Journal of the American Chemical Society, 1952. **74**(3): p. 719-722.
8. Zhang, J.G., et al., *Growth and spectral characterization of beta-Ga₂O₃ single crystals*. Journal of Physics and Chemistry of Solids, 2006. **67**(12): p. 2448-2451.
9. Villora, E.G., et al., *Large-size beta-Ga₂O₃ single crystals and wafers*. Journal of Crystal Growth, 2004. **270**(3-4): p. 420-426.
10. Vasylytsiv, V.I., Y.I. Rym, and Y.M. Zakharko, *Optical absorption and photoconductivity at the band edge of beta-Ga_{2-*x*}In_{*x*}O₃*. Physica Status Solidi B-Basic Research, 1996. **195**(2): p. 653-658.
11. Ueda, N., et al., *Synthesis and control of conductivity of ultraviolet transmitting beta-Ga₂O₃ single crystals*. Applied Physics Letters, 1997. **70**(26): p. 3561-3563.
12. Tamm, Y., et al., *Czochralski grown Ga₂O₃ crystals*. Journal of Crystal Growth, 2000. **220**(4): p. 510-514.
13. Suzuki, N., et al., *Fabrication and characterization of transparent conductive Sn-doped beta-Ga₂O₃ single crystal*. Physica Status Solidi C - Current Topics in Solid State Physics, Vol 4 No 7 2007, 2007. **4**(7): p. 2310-+.
14. Irmscher, K., et al., *Electrical properties of beta-Ga₂O₃ single crystals grown by the Czochralski method*. Journal of Applied Physics, 2011. **110**(6).
15. Yang, D., et al., *Selective Area Growth of Single-*

- Crystalline Alpha-Gallium Oxide on a Sapphire Nanomembrane by Mist Chemical Vapor Deposition*. *Acs Applied Electronic Materials*, 2021. **3**(10): p. 4328–4336.
16. Yang, D., et al., *Epitaxial Growth of Alpha Gallium Oxide Thin Films on Sapphire Substrates for Electronic and Optoelectronic Devices: Progress and Perspective*. *Electronic Materials Letters*, 2022. **18**(2): p. 113–128.
 17. Shinohara, D. and S. Fujita, *Heteroepitaxy of corundum-structured alpha-Ga₂O₃ thin films on alpha-Al₂O₃ substrates by ultrasonic mist chemical vapor deposition*. *Japanese Journal of Applied Physics*, 2008. **47**(9): p. 7311–7313.
 18. Lee, S.D., K. Akaiwa, and S. Fujita, *Thermal stability of single crystalline alpha gallium oxide films on sapphire substrates*. *Physica Status Solidi C: Current Topics in Solid State Physics*, Vol 10, No 11, 2013. **10**(11): p. 1592–1595.
 19. Varley, J.B., et al., *Role of self-trapping in luminescence and p-type conductivity of wide-band-gap oxides*. *Physical Review B*, 2012. **85**(8).
 20. Giovane, L.M., et al., *Correlation between leakage current density and threading dislocation density in SiGe p-i-n diodes grown on relaxed graded buffer layers*. *Applied Physics Letters*, 2001. **78**(4): p. 541–543.
 21. Kim, J., et al., *Linearly polarized photoluminescence of anisotropically strained c-plane GaN layers on stripe-shaped cavity-engineered sapphire substrate*. *Applied*

- Physics Letters, 2018. **112**(21).
22. Jang, J., et al., *Solid-phase epitaxy of a cavity-shaped amorphous alumina nanomembrane structure on a sapphire substrate*. Journal of Crystal Growth, 2018. **498**: p. 130–136.
 23. Jang, J., et al., *Incorporation of air-cavity into sapphire substrate and its effect on GaN growth and optical properties*. Journal of Crystal Growth, 2015. **430**: p. 41–45.
 24. Van de Walle, C.G. and J. Neugebauer, *First-principles calculations for defects and impurities: Applications to III-nitrides*. Journal of Applied Physics, 2004. **95**(8): p. 3851–3879.
 25. Kim, Y.W., et al., *Epitaxial (Gaas)_{1-X}(Si₂)_X Metastable Alloys on Gaas(001) and (Gaas)_{1-X}(Si₂)_X/Gaas Strained-Layer Superlattices – Crystal-Growth, Spinodal Decomposition, and Antiphase Domains*. Journal of Applied Physics, 1994. **76**(3): p. 1644–1655.
 26. Oshima, Y., et al., *Epitaxial lateral overgrowth of α -Ga₂O₃ by halide vapor phase epitaxy*. APL Materials, 2019. **7**(2).
 27. Jinno, R., et al., *Enhancement of epitaxial lateral overgrowth in the mist chemical vapor deposition of α -Ga₂O₃ by using a -plane sapphire substrate*. Japanese Journal of Applied Physics, 2019. **58**(12).
 28. Segura, A., et al., *Band gap of corundumlike α -Ga₂O₃ determined by absorption and ellipsometry*. Physical Review Materials, 2017. **1**(2).

29. Jamwal, N.S. and A. Kiani, *Gallium Oxide Nanostructures: A Review of Synthesis, Properties and Applications*. Nanomaterials, 2022. **12**(12).
30. Lee, S.D., et al., *Enhanced thermal stability of alpha gallium oxide films supported by aluminum doping*. Japanese Journal of Applied Physics, 2015. **54**(3).
31. Mondal, A.K., et al., *First-Principles Studies for Electronic Structure and Optical Properties of p-Type Calcium Doped alpha-Ga(2)O(3)*. Materials (Basel), 2021. **14**(3).
32. Pennycook, S.J., *Z-Contrast Transmission Electron-Microscopy - Direct Atomic Imaging of Materials*. Annual Review of Materials Science, 1992. **22**: p. 171-195.
33. Browning, N.D., M.F. Chisholm, and S.J. Pennycook, *Atomic-Resolution Chemical-Analysis Using a Scanning-Transmission Electron-Microscope*. Nature, 1993. **366**(6451): p. 143-146.
34. Zuo, J.M., et al., *Lattice and strain analysis of atomic resolution Z-contrast images based on template matching*. Ultramicroscopy, 2014. **136**: p. 50-60.
35. Phillips, P.J., et al., *Atomic-resolution defect contrast in low angle annular dark-field STEM*. Ultramicroscopy, 2012. **116**: p. 47-55.
36. Perovic, D.D., C.J. Rossouw, and A. Howie, *Imaging Elastic Strains in High-Angle Annular Dark-Field Scanning-Transmission Electron-Microscopy*. Ultramicroscopy, 1993. **52**(3-4): p. 353-359.

37. Shapenkov, S., et al., *Halide Vapor Phase Epitaxy alpha- and epsilon-Ga(2)O(3) Epitaxial Films Grown on Patterned Sapphire Substrates*. Physica Status Solidi a-Applications and Materials Science, 2020. **217**(14).
38. Polyakov, A.Y., et al., *Deep trap spectra of Sn-doped alpha-Ga2O3 grown by halide vapor phase epitaxy on sapphire*. Apl Materials, 2019. **7**(5).
39. Ghadbeigi, L., et al., *Optical Characterization of Gallium Oxide alpha and beta Polymorph Thin-Films Grown on c-Plane Sapphire*. Journal of Electronic Materials, 2021. **50**(6): p. 2990-2998.

Chapter 5. Conclusion

Cathodoluminescence analysis of high-energy UV region below 300nm was conducted in a transmission electron microscope by using a home-built deep UV CL stage. We would expand detection limit from 350nm to 200nm using a Custom-made fused silica lens. To increase reflectance, we adopt an electrolytic polishing method. The perfect mirror is formed without deformation of the calculated curvature.

Also, the light collectible TEM stage was combined with a liquid nitrogen cooling system. Combination with the cooling system make increased light emitting efficiency and give us more detailed spectral information of the sample.

The performance and applicability of deep UV CL stage was successfully demonstrated by analyzing alpha Ga₂O₃.

A high-quality alpha-Ga₂O₃ thin film was grown on the membrane of the Al₂O₃ single-crystal substrate. Hetero-epitaxial alpha Ga₂O₃ crystals are nucleated and grown with 3-fold symmetry based on the template provided by Al₂O₃. The APD confirmed by CBED is believed to be developed at the stage of nucleation based on the unstable, or uneven Al-O templates provided by the Al₂O₃ surface.

The Most stable stacking sequence are A'B'(Al₂O₃)/ (Ga₂O₃)AC-BA-

CB and A'B'(Al₂O₃)/(Ga₂O₃)CB-AC-BA, which is supported by DFT calculation and experiment results. The domain and APD boundaries exhibit bright contrast in ADF, which originates from local strain and not from the local elemental concentration of gallium.

They were found to have 180-degree inverted configurations from the surroundings. These APDs lead to sub-diffraction spots when observed along [110] and [010], and can identify using higher-order Laue zone reflections in CBED.

As confirmed by CL measurement in TEM, the bandgap energy of alpha-Ga₂O₃ is inferred to be 5.56 eV with a near band edge transition of ~ 223nm. Although the height and position of peaks vary slightly changes from area to area, the luminescence peaks at 320nm, 380nm, 410nm, 440nm, and 470nm are commonly observed throughout the crystal - inside domain, domain boundary, and APD boundary - but the APD boundary exhibits the 350nm peak. The transition results from intermediate states generated by strain induced by the coalescing domain boundaries.

Curriculum Vitae

Yong-Hee Lee

In-situ Electron Microscopy Laboratory

Department of Materials Science and Engineering

Seoul National University

E-mail : lyh87@snu.ac.kr

Tel:+82-2-878-5010 Fax:+82-2-878-5010

■Education

- | | |
|-----------------------|---------------------------------------------------------------------------------------------------------------------------------------------------------------------------|
| Sep. 2014 – Present | Integrated MA/Ph.D course, Department of
Materials Science and Engineering, Seoul National
University, Seoul, Republic of Korea
(Advisor : Prof. Young-woon Kim) |
| Mar. 2007 – Aug. 2013 | B.S., Department of Digital Display Engineering,
Hoseo University, Asan, Republic of Korea |

■Research Experiences

• TEM-CL System Development

- Development of a home-built TEM-CL stage for DEEP UV range
- Development of a home-built TEM-CL stage for Infrared range

• TEM-CL analysis of semiconducting materials

- TEM-CL analysis of anti-phase domain boundary in the α -Ga₂O₃ thin films
- TEM-CL analysis of dry etching damage in the InGaN micro LED
- TEM-CL analysis of quantum well thickness fluctuation in the InGaN single quantum well LED
- TEM-CL analysis of crystal structure of Hf-O in the Hf-O thin films
- TEM-CL analysis of nanostructure materials such as ZnO nano-wires,

perovskite quantum dot LED

- TEM-CL analysis of two-dimensional electron gas in SiC HEMT

- **Microstructure analysis using electron microscopes**

- Microstructure analysis of extra diffraction spots in α -Ga₂O₃ thin films
- Microstructure analysis of anti-phase domain and boundary in α -

Ga₂O₃ thin Films

- Microstructure analysis of dry etching damage in the InGaN micro LED
- Microstructure analysis of ZnO nano-wires
- Microstructure analysis of SiC HEMT
- TEM analysis of crystal structure of polycrystalline β -Ga₂O₃ thin films
- TEM analysis of crystal structure of polycrystalline Hf-O₂ thin films

■ Experimental Skills

- **Preparation of TEM specimen**

- Mechanical polishing & Ion milling (PIPS, Gatan)

- **Transmission Electron Microscope (TEM) Operation**

- Instrument: JEM-200CX, JEM-3000F, JEM-2010F, Technai-F20, Themis-Z
- Techniques: high-resolution(HR) imaging, bright field (BF) dark field (DF) imaging, weak beam dark field imaging (WBDF), convergent beam electron diffraction (CBED), selected area diffraction (SAD), nanobeam electron diffraction(NBD), scanning transmission electron microscopy(STEM), energy dispersive x-ray spectroscopy (EDS), cathodoluminescence (CL), atomic-resolution (S)TEM imaging, 4D STEM

- **Scanning Electron Microscope (SEM) Operation**

- Instrument: JSM-6390LV, JSM-5600
- Techniques: secondary electron (SE) imaging, back-scattered electron (BSE)imaging, energy dispersive x-ray Spectroscopy(EDS), cathodoluminescence (CL)

- **Focus Ion Beam (FIB) Operation**

- Instrument: SMI3050SE (SII Nanotechnology)
- **X-ray Diffraction (XRD) Operation**
 - Instrument: X`Pert Pro (PANalytical)
- **EM simulation tools**
 - JEMS (EMS electron microscopy simulation program), Crystal maker (atomic model simulation program), VESTA (atomic model simulation program), QSTEM (Atomic-resolution STEM and diffraction plane simulation program), CASINO (Monte-Carlo simulation program)
- **Image editing tools**
 - ImageJ (Image stack generation and editing), GMS(Gatan Digital Micrograph), Camtasia(Movie making), VirtualDub(Movie editing)
- **Instrument design tools**
 - Autodesk Inventor (3D design), Autodesk AutoCAD (2D design)
- **Setup and Operation of vacuum chamber**
 - Instrument: PECVD, LPCVD, Sputter, Evaporator, Etcher, IMD
 - Set up a multi-functional vacuum chamber for vacuum annealing and thermal evaporation and sputtering with rotary pump, turbo pump to 10⁻⁷ torr vacuum range

■ List of Publications

1. **Yong-Hee Lee**, Byeongjum Gil, Duyoung Yang, Mi-Hyang Sheen, Euijoon Yoon, Yongho Park, Ho Won Jang, Sangmoon Yoon, Miyoung Kim, Young-Woon Kim, “Luminescence properties related anti-phase domain of alpha-Ga₂O₃”, *APL Materials*. 11, 051113 (2023)
2. **Yong-Hee Lee**, Duyoung Yang, Byeongjum Gil, Mi-Hyang Sheen, Euijoon Yoon, Yongho Park, Ho Won Jang, Sangmoon Yoon, Miyoung Kim, Young-Woon Kim, “Origin of extra diffraction spots in high crystalline alpha-Ga₂O₃”, *AIP Advances*. 13, 025148 (2023)
3. Young-Hoon Kim, Sungjin Kim, Arvin Kakekhani, Jinwoo Park, Jaehyeok

- Park, **Yong-Hee Lee**, Hengxing Xu, Satyawan Nagane, Robert B. Wexler, Dong-Hyeok Kim, Seung Hyeon Jo, Laura Martínez-Sarti, Peng Tan, Aditya Sadhanala, Gyeong-Su Park, Young-Woon Kim, Bin Hu, Henk J. Bolink, Seunghyup Yoo, Richard H. Friend, Andrew M. Rappe, Tae-Woo Lee " Comprehensive defect suppression in perovskite nanocrystals for high-efficiency light-emitting diodes ", *Nature Photonics*. 15, 148–155 (2021)
4. Yongsub Kim, Bosung Kim, Biswanath Bhoi, **Yong Hee Lee**, Young-Woon Kim, Sang-Koog Kim " Annealing effect of sputter-grown Pt/Ni₈₀Fe₂₀/Pt sandwich trilayer films on Gilbert damping ", *Journal of Applied Physics*. 128, 223901 (2020)
 5. Hee Jae Chae, Hyung Yoon Kim, Sol Kyu Lee, Ki Hwan Seok, **Yong-Hee Lee**, Zohreh Kiaee, Seung Ki Joo " Effect of Ultrathin Silicon Oxide Film for Enhanced Performance and Reliability of Metal-Induced Laterally Crystallized Thin-Film Transistors Using Silicon Nitride as a Gate Dielectric ", *ECS J. Solid State Sci. Technol.* 5 Q279 (2016)
 6. Hyung Yoon Kim, Jae Hyo Park, Ki Hwan Seok, Zohreh Kiaee, Hee Jae Chae, Sol Kyu Lee, **Yong Hee Lee**, Jae Ho Lee, Seung Ki Joo " Thermal Stress Effect on Nickel Silicide Seed-Induced Laterally Crystallized Polycrystalline-Silicon Thin-Film Transistors ", *Journal of nanoscience and Nanotechnology*, Volume 16, Number 9, (2016)
 7. Hyung Yoon Kim, Ki Hwan Seok, Zohreh Kiaee, Hee Jae Chae, Sol Kyu Lee, **Yong Hee Lee**, Jae Ho Lee, Seung Ki Joo " Novel Fabrication of Lightly Doped-Drain for Suppressing the Leakage Current in Polycrystalline Silicon Thin-Film Transistor ", *Journal of nanoscience and Nanotechnology*, Volume 17, Number 5, (2017)
 8. Sol Kyu Lee, Ki Hwan Seok, Hyung Yoon Kim, Zohreh Kiaee, Hee Jae Chae, **Yong-Hee Lee**, and Seung Ki Joo " Advanced Four-Mask Process Bottom-Gate Poly-Si TFT via Self-Aligned NiSi₂ Seed-Induced Lateral Crystallization ", *IEEE ELECTRON DEVICE LETTERS*, VOL. 37, NO. 10,

(2016)

9. Sol Kyu Lee, Ki Hwan Seok, Jae Hyo Park, Hyung Yoon Kim, Hee Jae Chae, Gil Su Jang, **Yong-Hee Lee**, Ji Su Han, Seung Ki Joo " Progress of p-channel bottom-gate poly-Si thin-film transistor by nickel silicide seed-induced lateral crystallization ", *Applied Physics A*, 122, 613 (2016)
10. Ki Hwan SEOK, Hyung Yoon Kim, Jae Hyo Park, Sol Kyu Lee, **Yong-Hee Lee**, Seung Ki Joo " Edge Cut Process for Reducing Ni Content at Channel Edge Region in Metal Induced Lateral Crystallization Poly-Si TFTs ", *JSTS:Journal of Semiconductor Technology and Science*, vol. 16, no. 2. (2016)
11. Jae Hyo Park, Ki Hwan Seok, Hyung Yoon Kim, Sol Kyu Lee, Hee Jae Chae, **Yong Hee Lee**, Jae Ho Lee, Zohreh Kiaee, Donghwan Ahn, Seung Ki Joo " Compressive Stressed P-Channel Polycrystalline-Silicon Thin-Film Transistors for High Field-Effect Mobility ", *IEEE ELECTRON DEVICE LETTERS*, VOL. 36, NO. 8, (2015)
12. Jae Hyo Park, Hyung Yoon Kim, Ki Hwan Seok, Zohreh Kiaee, Sol Kyu Lee, Hee Jae Chae, **Yong Hee Lee**, Jae Ho Lee, Seung Ki Joo " Retrograde-Mask Processed Polysilicon TFT for High Performance, Planar Structure, and Stable Operation ", *IEEE ELECTRON DEVICE LETTERS*, VOL. 36, NO. 8, (2015)
13. Jae Hyo Park, Hyung Yoon Kim, Ki Hwan Seok, Hee Jae Chae, Sol Kyu Lee, **Yong Hee Lee**, Zohreh Kiaee, Seung Ki Joo " Tempered glass substrate effect on the growth of polycrystalline-silicon and its applications for reliable thin-film transistors ", *RSC Adv.*, 2015, 5, 55909-55913

Abstract (in Korean)

본 논문에서는 투과전자현미경에서 이용 가능한 고에너지 자외선 영역용 음극형광 system을 제작 및 활용하여 고 결정성 $\alpha\text{-Ga}_2\text{O}_3$ 에 존재하는 anti-phase domain이 발광 특성에 미치는 영향에 대해 연구하였다. 분석하여 물질의 밴드갭 에너지 구조에 관한 정보를 제공한다.

첫째, 투과전자현미경 내에서 고에너지 자외선영역(DUV)을 측정할 수 있는 음극형광(CL) 분석법을 개발하였다. 투과전자현미경 내에서 음극형광 분석이 가능한 stage를 제작하려면 사용되는 모든 부품(미러, 렌즈, 광섬유 등)은 objective pole piece gap인 3mm보다 작아야 한다. 현재 3mm 이내 크기로 상용화된 렌즈는 BK7 소재이고, 350nm의 cut-off range를 갖고 있어서 고 에너지 영역을 탐지할 수 없다. 고 에너지 자외선 영역을 탐지하기 위해 Fused silica 소재로 lens를 맞춤 제작하였고, detection limit을 200nm까지 확장하였다. 또한 음극형광에 의해 발생된 빛을 최소의 손실로 분광기로 전달하기 위해 다음과 같은 방법을 사용하여 시스템을 최적화하였다.

(i) 고 에너지 영역에서 높은 반사도를 갖는 알루미늄 소재를 사용하였고, 전해 연마를 통해 계산된 곡률의 변형없이

완벽한 경면을 완성하였다. (ii) 감쇄 효율이 제일 낮은 광섬유를 사용하여 손실을 최소화하였다. (iii) 고 에너지 자외선 영역의 양자 효율이 최대가 될 수 있는 grating과 CCD를 사용하였다. (iv) 음극형광에 의해 발생하는 빛의 양을 증가시키고 분광 분해능을 향상시키기 위해 액화질소를 활용한 냉각 시스템을 장착하였다.

둘째, 다양한 투과전자현미경 분석 기법을 활용하여 고 결정성 $\alpha\text{-Ga}_2\text{O}_3$ 에서 관찰되는 추가 회절점의 원인이 anti-phase domain(APD)라는 점을 밝혔다. 엑스레이 회절 분석을 통해 확인된 고 결정성 $\alpha\text{-Ga}_2\text{O}_3$ 에서 [110], [010] 그리고 [221] zone에서 추가 회절점이 관찰된다. 하지만 [001] zone에서 촬영 시 추가 회절점이 관찰되지 않았다.

[001] zone에서 관찰되지 않는 원인을 찾기 위해 [221] zone의 암시야상 이미지에서 추가 회절점이 관찰되는 영역에 집속된 전자빔을 조사하여 기준점을 만들었다. 생성된 기준점 주변을 [001] zone으로 기울여 촬영한 ADF Image에서 다양한 크기의 domain들이 관찰되었다. domain들간의 결정 구조의 연관성은 Converged beam electron diffraction(CBED) 기법을 통해 분석하였다. CBED 결과 분석을 통해 추가 회절점이 관찰되는 영역에서 APD이 존재하는 것이 확인되었다.

Ga_2O_3 은 3-fold symmetry를 갖는 물질로서 120도 마다

동일한 원자 구조를 갖는다. 하지만 60도 회전되면 회전하기 전의 원자 구조와 다른 구조가 관찰되고, 이 구조는 180도 반전된(APD)구조와 일치한다. APD와 추가 회절점의 연관성을 확인하기 위해 원자 구조 분석과, atomic-resolution ADF image 분석을 진행하였다. 추가 회절점이 관찰되는 영역의 atomic-resolution ADF 이미지를 확인해보면 기판과 동일한 적층 구조로 성장된(IPD)영역의 원자 이미지와 다른 것이 확인되고, 일정한 주기를 갖는 밝은 Ga 원자가 관찰된다. IPD과 APD의 [110] zone 원자 구조를 비교해보면 c축 방향으로 60도 기울어진 구조를 갖는다. IPD 와 APD의 원자 구조를 겹쳐보면 추가 회절점이 관찰되는 영역의 atomic-resolution image와 일치하는 것을 알 수 있다. 두 원자구조를 겹칠 경우 두 원자의 구조가 다르기에 Ga 원자는 동일한 위치, 또는 어긋난 위치에 있게 된다. 동일한 위치에서 겹쳐지게 되면 어긋난 위치에 있는 것보다 한 곳에 Ga 원자의 비중이 더 커진다. 이에 ADF image의 Z-contrast가 밝게 관찰되고, 밝게 관찰되는 Ga의 주기성으로 인해 추가 회절점이 발생된다. 추가 회절점이 [001] zone에서는 존재하지 않는다는 것은 추가 회절점이 APD에 의해 발생된다는 또다른 근거이다. [001] 방향에서는 두 원자 구조가 겹쳐지지 않기 때문이다.

셋째, 다양한 투과전자현미경 분석 기법을 활용하여 고

결정성 $\alpha\text{-Ga}_2\text{O}_3$ 에 존재하는 APD의 생성 원인을 밝혔다. APD의 발생 원인을 찾기 위해 Al_2O_3 와 Ga_2O_3 계면의 atomic-resolution ADF image 분석과 원자 구조 분석, Al_2O_3 의 oxygen termination layer 원자 구조 분석 그리고 DFT 계산을 통한 formation energy 분석을 진행하였다.

기판인 Al_2O_3 와 IPD Ga_2O_3 의 Al과 Ga은 정삼각형 산소 위에 위치한다. APD 경계의 원자 구조 분석을 통해 APD 또한 IPD와 동일하게 정삼각형 산소 위에 위치하는 것을 확인하였다. 정삼각형 산소 위로 적층되면서 180도 반전(혹은 60도 회전된)될 수 있는 3가지 원자 구조 domain stacking(DS) 2($\text{A}^{\text{B}}(\text{Al}_2\text{O}_3)/(\text{Ga}_2\text{O}_3)\text{BA} - \text{CB} - \text{AC}$), DS3 ($\text{A}^{\text{B}}(\text{Al}_2\text{O}_3)/(\text{Ga}_2\text{O}_3)\text{AC} - \text{BA} - \text{CA}$), DS4($\text{A}^{\text{B}}(\text{Al}_2\text{O}_3)/(\text{Ga}_2\text{O}_3)\text{CB} - \text{AC} - \text{BA}$)의 formation energy를 계산하였고, DS3 와 DS4 두 원자 구조가 동일하게 낮은 formation energy를 갖는 것을 확인하였다. atomic-resolution image를 통해 DS3 와 4만 존재하는 것을 검증하였다. 또한, 산소 공공이 존재할 때의 formation energy 계산을 통해 APD은 산소 공공에 의해 발생될 수 있음을 확인하였다. 마지막으로, 개발된 DUV TEM CL 시스템을 활용하여 APD이 발광 특성에 미치는 영향을 분석하였다. 음극형광 이미지를 확인해보면 320nm

파장에서 도메인 내부가, 380-480nm 파장 영역에서 도메인 경계면들이, 350nm 파장에서 특정한 도메인 경계면이 밝게 관찰된다. 동일한 위치의 ADF 이미지를 확인해보면 350nm, 380-480nm 파장에서 밝게 관찰되는 위치에 밝은 경계면이 확인된다. ADF 이미지에서 밝게 관찰되는 경계면의 경우 Ga원자의 비중이 더 높을 것이라 예상됐지만, EELS 원소 분석, 경계면의 원자 구조 분석, ADF 이미지의 수집각 변화를 통해 Strain에 의해 발생된 것을 확인하였다. 또한 350nm에서 밝게 관찰되는 경계면은 CBED 통해 APD 경계면이라는 것을 확인하였다. APD 경계면과 도메인 경계면의 차이를 확인하고자, pristine bulk와 APD boundary 원자 구조를 DFT 계산을 진행하였다. 계산에 사용된 APD boundary 원자 구조는 경계면의 원자 구조와 APD 적층 구조 분석을 통해 도출하였다.

APD 경계면의 경우 Pristine bulk에 존재하지 않는 결합 준위가 valance band 근처에서 생성되는 것을 확인하였다. 생성된 결합 준위와 350nm 파장의 에너지가 동일하지는 않기에 350nm는 conduction band to trap transition은 아니라고 생각된다. 하지만 APD 경계면에서 새로운 결합 준위가 발생되므로, 350nm는 APD에서 기인한 trap to trap transition에 의한 peak임을 알 수 있다.

주요어 : 음극형광, 고 에너지 자외선 영역, 투과전자현미경, 발광
특성, 산화갈륨, 역 결정상, 추가 회절점

학 번 : 2014-22526

이 용 희